

Beyond prewhitening: detection of gravity modes and their period spacings in slowly pulsating B stars using the multitaper F-test

Aarya A. Patil^{1,*}, Conny Aerts^{1,2,3}, Nikki Y. N. Wang¹, Jordan Van Beeck⁴, and May G. Pedersen^{5,6}

¹ Max-Planck-Institut für Astronomie, Königstuhl 17, D-69117 Heidelberg, Germany
e-mail: patil@mpia.de

² Institute of Astronomy, Department of Physics & Astronomy, KU Leuven, Celestijnenlaan 200 D, 3001 Leuven, Belgium
e-mail: conny.aerts@kuleuven.be

³ Department of Astrophysics, IMAPP, Radboud University Nijmegen, PO Box 9010, 6500 GL Nijmegen, The Netherlands

⁴ Heidelberg Institute for Theoretical Studies, Schloss-Wolfsbrunnengasse 35, 69118 Heidelberg, Germany

⁵ Sydney Institute for Astronomy, School of Physics, University of Sydney, Sydney, NSW 2006, Australia

ABSTRACT

Gravity modes in main-sequence stars have traditionally been studied using a prewhitening approach, which iteratively identifies modes in the Fourier domain and subsequently tunes their frequencies, amplitudes, and phases through time-domain regression. While effective, this method becomes inefficient when analysing large volumes of long time-series data and often relies on subjective stopping criteria to determine the number of iterations. We aim to perform frequency extraction of gravity modes in slowly pulsating B (SPB) stars using a statistically robust, data-driven approach based on advanced power spectrum and harmonic analysis techniques. Our approach employs the multitaper non-uniform fast Fourier transform, mtNUFFT , a power spectrum estimator that addresses several statistical limitations of traditional methods such as the Lomb-Scargle periodogram. We apply its extension, the multitaper F-test, to extract coherent gravity modes from 4-year *Kepler* light curves of SPB stars and to search for period spacing patterns among the extracted modes. The multitaper F-test enables fast and accurate extraction of the properties of gravity modes with quasi-infinite lifetimes, preferentially selecting modes that exhibit purely periodic behaviour. Although the method typically extracts fewer frequencies than conventional prewhitening, it recovers most known modes and, in some cases, reveals new ones. We also find evidence for gravity modes with long but finite lifetimes, and detect more than one period spacing pattern in some of the studied SPB stars. Overall, the multitaper F-test offers a more objective and statistically sound alternative to prewhitening. It scales efficiently to large datasets containing thousands of pulsators, and has the potential to facilitate mode identification and to distinguish between the different excitation mechanisms operating in SPB stars.

Key words. Asteroseismology – Waves – Stars: oscillations (including pulsations) – Stars: interiors – Techniques: photometric – Methods: Statistical

1. Introduction

The power spectra of slowly pulsating B (SPB) stars reveal rich patterns of high-radial-order, low-degree ($l \lesssim 2$) gravity (g) mode oscillations. These stars have masses in the range of approximately $3\text{--}9M_{\odot}$ and cover the entire main-sequence evolution (Aerts et al. 2010). The g-mode pulsations in these stars are driven by the κ -mechanism (also called the heat-engine mechanism), which operates in the iron-group opacity bump within the stellar radiative envelopes (Pamyatnykh 1999). While we know that rotation has a substantial effect on their mode excitation (Townsend 2005a,b; Szewczuk & Daszyńska-Daszkiewicz 2017), the impact of other internal physical aspects is not well understood (e.g., Rehm et al. 2024). Moreover, we know that current instability computations predict overly restricted mode excitation regions in the Hertzsprung–Russell diagram, that is, the regions where stars are theoretically expected to exhibit excited modes. This became clear since the *Gaia* mission delivered light curves for thousands of g-mode pulsators in the main-sequence phase (Gaia Collaboration et al. 2023). These numerous newly discovered pulsators have well-determined astrophysical properties by now (Aerts et al. 2023; Hey & Aerts 2024),

leading to the conclusion that g-mode pulsators cover the entire mass range from $1.3M_{\odot}$ to about $9M_{\odot}$ along the main sequence (Mombarg et al. 2024; Aerts et al. 2025).

Aside from the incomplete understanding of mode excitation in BAF-type stars, angular momentum transport inside such stars and their successors at different evolutionary stages remains poorly understood. On the one hand, Aerts et al. (2019) deduced that angular momentum transport happens more efficiently than predicted by current theories when stars have a convective core. On the other hand, if g modes themselves play a role in angular momentum transport, it seems to happen too efficiently and on too short time scales in SPB stars (Townsend et al. 2018). Proper measurements of non-linear resonant mode coupling (Van Beeck et al. 2024) and g mode lifetimes in SPB stars are essential to improve the interpretation of mode excitation and to evaluate the role of these modes in active transport processes.

The coherent, heat-driven g modes in SPB stars are assumed to have quasi-infinite lifetimes, producing sharp, nearly delta-function-like peaks in the frequency domain signal (power spectrum). Such signals differ from the broader Lorentzian profiles characteristic of damped modes observed in sun-like stars (García & Ballot 2019) or in red giants (Hekker & Christensen-Dalsgaard 2017) with a substantial convective envelope. How-

* LSST-DA Catalyst Fellow

ever, modern space photometry has revealed additional stochastic low-frequency variability alongside the coherent modes in several SPB stars and in more massive OB-type stars (Blomme et al. 2011; Neiner et al. 2012; Tkachenko et al. 2014; Aerts & Rogers 2015; Aerts et al. 2018a; Ramiaramanantsoa et al. 2018; Pedersen et al. 2019; Bowman et al. 2019; Burssens et al. 2020; Bowman et al. 2020; Szewczuk et al. 2021; Elliott et al. 2022; Bowman et al. 2024; Zhang et al. 2024; Shen et al. 2024; Kourmiotis et al. 2025; Pedersen & Bildsten 2025). This low-frequency variability has been interpreted as either damped gravity or gravito-inertial waves excited stochastically at the convective core boundary (Edelmann et al. 2019; Ratnasingam et al. 2020; Horst et al. 2020; Ratnasingam et al. 2023; Vanon et al. 2023) or through sub-surface convective motions (Cantiello et al. 2009; Lecoanet et al. 2019; Schultz et al. 2022; Anders et al. 2023). A third possible explanation is variability induced by stellar winds (Krtićka & Feldmeier 2018, 2021).

High-resolution spectroscopic measurements of macroturbulence provide another manifestation of such low-frequency variability (Simón-Díaz et al. 2017). Yet the observed macroturbulent spectral line broadening cannot be fully attributed to sub-surface convection across the entire SPB mass range, because B stars of later spectral type lack the appropriate sub-surface convection zones (Cantiello & Braithwaite 2019). However, a plausible explanation for the low-frequency variability observed in such SPB stars is the presence of internal gravity waves. These waves can tunnel through the evanescent zone adjacent to the mode cavity to be able to reach the surface (Serebriakova et al. 2024). Clearly, there is a need to unravel which of the detected periodic peaks in the frequency spectra of SPB pulsators are due to coherent modes and which ones can be ascribed to internal gravity waves travelling through parts of the interior all the way up to the surface.

Traditionally, the Lomb-Scargle (LS) periodogram is applied to space-based photometric time-series of pulsating stars to estimate their power spectra, followed by an iterative “prewhitening” procedure to extract individual frequencies of modes whose lifetimes are much longer than the time-series data. The standard prewhitening approach in the literature (see e.g., Breger et al. 1993; Antoci et al. 2019, for ground- and space-based photometric light curves, respectively) iteratively combines frequency extraction in the Fourier domain with least-squares fitting in the time domain to optimize the description of the light curve. The reason for optimization in the time domain is that the LS periodogram estimates the total power in a time-series that can be attributed to a given frequency without distinguishing between a purely periodic and a quasi-periodic signal. The mtNUFFT framework introduced by Patil et al. (2024), when combined with the multitaper F-test (Patil et al. 2025), makes this distinction. Thus, the mtNUFFT/F-test methodology appears particularly well-suited for detecting coherent (undamped) modes with quasi-infinite lifetimes and long-lived yet damped gravity waves, potentially outperforming traditional techniques for detecting and distinguishing these different types of signals. The current paper exploits this potential for the case of SPB pulsators.

2. Targets and starting point of our approach

This study is a pilot bridging statistical techniques in time-series analysis and the need to extract mode frequencies and mode lifetimes while avoiding data manipulation in an iterative process. For various reasons, the class of SPB pulsators is an optimal population to test our approach via the multitaper F-test.

They have 4 years-long *Kepler* light curves of high quality that serve as the best available observational basis for detailed asteroseismology (Gilliland et al. 2010; Pápics et al. 2014, 2015). The SPB pulsators have numerous coherent g modes of low degree and consecutive radial order with beating patterns of years-long duration. The numerous excited modes can be dissected and turned into period spacing patterns (Degroote et al. 2010a; Pápics et al. 2014, 2015, 2017; Pedersen et al. 2021; Zhang et al. 2018; Szewczuk & Daszyńska-Daszkiewicz 2018; Szewczuk et al. 2021, 2022).

The morphology of diagrams that plot the period spacings versus the periods of modes having consecutive radial order for the same degree and azimuthal order, allows us to determine stellar internal rotation in a model-independent way. In particular, one estimates the slopes of these period spacing patterns to determine the internal rotation frequency in the region between the convective core and the radiative envelope. This can be done numerically using the methods developed by Van Reeth et al. (2015a, 2016) and by Christophe et al. (2018), delivering at once the identification of the degree and azimuthal order of the modes. Moreover, constraints on internal mixing can be achieved using structures and dips in the observed patterns post mode identification, as predicted from theory by Miglio et al. (2008); Bouabid et al. (2013); Pedersen et al. (2018); Aerts et al. (2018b); Michielsen et al. (2019). Finally, internal magnetic fields in these B stars leave measureable imprints on their g-mode frequencies, with the extent of frequency variations depending on both magnetic field strength and stellar rotation rate (Aerts et al. 2021; Lecoanet et al. 2022).

While the forward asteroseismic modelling methods based on g modes in main-sequence stars are well developed and their potential for probing the internal physics is clear (Aerts 2021), applications to SPB stars remain limited. This is largely because prewhitening applied to *Kepler* photometry delivers a lot of frequencies but filtering out the coherent modes and constructing period spacing patterns is challenging. An important aspect of this challenge is that some of the modes are not coherent but rather seem to be damped travelling low-frequency waves or modes with lifetimes shorter than or similar to the duration of the observations. Moreover, some of the investigated SPB stars show outbursts in their light curves possibly due to nonlinearly coupled modes (Van Beeck et al. 2021, referred to as VB21 hereafter), as has also been observed in fast rotating pulsating Be stars (Neiner et al. 2009, 2020). Due to these challenges, the sample of SPB and Be stars with detailed asteroseismic modelling is too limited and we do not have unbiased population studies yet to help improve stellar evolution models (Neiner et al. 2012; Pedersen et al. 2021; Pedersen 2022). Thousands of pulsating B stars with excellent space photometric light curves remain uninterpreted due to the lack of mode identification (e.g., Balona et al. 2011; Hey & Aerts 2024; Sharma et al. 2022).

In this work, we try a different approach to extract mode frequencies, assess mode lifetimes, and search for period spacing patterns in SPB pulsators. We do so by applying the mtNUFFT/F-test method introduced in Patil et al. (2025). We test and evaluate the method on 38 SPB stars whose 4-year *Kepler* light curves were constructed by Pedersen (2020). Pedersen (2020) had a total sample of 60 SPB stars for which she performed lightcurve and Fourier analysis to look for period spacing patterns. She found period spacing patterns for 38 of the 60 stars, which we use in this paper. She used prewhitening to extract all the frequencies whose amplitudes exceed a local signal-to-noise ratio (SNR) of 4 in the LS periodogram and hunt for period spacing patterns, succeeding for 38 of the 60 SPB pulsators. She subse-

quently forward modelled 26 of the pulsators in Pedersen et al. (2021, hereafter PD21). Several of the 38 stars were identified as having multiple period spacing patterns, but Pedersen (2020) decided to focus on one pattern for each star and only model the identified dipole period spacing patterns in PD21.

The frequency extraction for the 38 SPB stars was revisited by VB21. They used five different prewhitening strategies to extract frequencies. In contrast to PD21, VB21 limited the extraction to a maximum of 200 frequencies per star per method, as their purpose was to study the impact of different stopping criteria on the interpretations of the frequency spectrum. Two of their methods were inspired by the approach developed by Van Reeth et al. (2015a) to hunt for period spacing patterns of g modes in γ Doradus pulsators, which have longer patterns than SPB stars (Van Reeth et al. 2015b; Li et al. 2020).

Here, we in turn revisit the results in VB21, assessing to what level the frequency values resulting from each of their five prewhitening strategies per star are the same or not. We deduce that the two strategies that select frequencies and initialise the optimisation using amplitude significance, which is inferred using either a likelihood ratio test or a Z-test, perform best for 34 of the 38 SPB pulsators treated by VB21. Using the frequencies passing the likelihood ratio test or Z-test leads to systematically better nonlinear harmonic regression models optimising the amplitude, frequency, and phase for each of the periodic signals in the time domain. In particular, these two approaches perform better than the traditional method of using an SNR stopping criterion as adopted in most frequency analyses of intermediate- and high-mass pulsators (e.g., Antoci et al. 2019; Pedersen et al. 2021).

Each prewhitening strategy in VB21 yields a separate regression model for every SPB star. For those models with an explained scaled variance (a measure of regression quality, defined in Eq. 3 of VB21) exceeding 90 %, most extracted frequencies agree within 3σ . Nevertheless, up to a handful of frequencies differ among the five regression models. Moreover, for the stars with regression models explaining less than 90% of the variance, the number of frequencies differing among the five methods increases as the explained variance decreases. Given these modest yet clear differences in the regression-model frequencies for each star arising from the five prewhitening approaches, we re-analyse the lightcurves constructed by Pedersen (2020) for the 38 SPB stars with our $\text{mtNUFFT}/\text{F-test}$ method. We use the exact same light curves as interpreted by PD21 and VB21 as the starting point of our work.

In addition to frequency-by-frequency comparisons, we also compare some period spacing patterns with those in PD21. These authors went further than VB21 in that more than 200 significant frequencies were considered in their regression models for most of the 26 SPB stars they interpreted asteroseismically. We compare the primary period spacing patterns we find with those of PD21 and also highlight the presence of candidate secondary patterns.

The results discussed below qualitatively show that our method improves upon the computational efficiency of previously used prewhitening approaches. We provide a unique way to pick out g modes with purely periodic behaviour, that is, modes with quasi-infinite lifetimes. Our results also suggest that some g modes are damped enough that their power spectra resemble those of damped harmonic oscillators as opposed to being delta functions. The damped nature of the modes will be considered in future work. Finally, we provide a method to detect as many independent frequencies as possible and present a

frequency-by-frequency as well as period spacing pattern comparison between our g-mode estimates and those in the literature.

3. Statistical analysis method

3.1. The mtNUFFT periodogram

In Patil et al. (2024), we introduce the mtNUFFT periodogram, which computes the power spectrum underlying a signal x_n sampled at quasi-regular times t_n , $n = \{0, \dots, N-1\}$ as the average of multiple *tapered* power spectrum estimates. We define it as

$$\hat{S}^{(\text{mt})}(f) = \frac{1}{K} \sum_{k=0}^{K-1} \hat{S}_k(f). \quad (1)$$

Here, $\hat{S}^{(\text{mt})}(f)$ denotes the average of K tapered estimates $\hat{S}_k(f)$ of order $k = 0, \dots, K-1$. These estimates are given by

$$\hat{S}_k(f) = |y_k(f)|^2, \quad (2)$$

where

$$y_k(f) = \sum_{n=0}^{N-1} v_{k,n}^* x_n e^{-i2\pi f t_n}. \quad (3)$$

Essentially, one estimates the k th-eigencoefficient $y_k(f)$ as described in Equation 3, the squared magnitude of which is the eigenspectrum $\hat{S}_k(f)$ in Equation 2. To estimate $y_k(f)$, the signal x_n is multiplied by the k th order taper $v_{k,n}^*$. The \star notation in the taper represents that the regularly-sampled taper $v_{k,n}$ is evaluated at quasi-regular times t_n (refer to Springford et al. 2020; Patil et al. 2024, for details on how these tapers are evaluated using interpolation). After tapering the signal, one applies the adjoint nonuniform fast Fourier transform (NUFFT) to compute the eigencoefficients $y_k(f)$ on a grid of frequencies $f \in [0, f_{\text{Nq}}]$, where f_{Nq} denotes the Nyquist frequency or the largest frequency measurable in the signal. While the Nyquist frequency is well-defined for regularly-sampled time-series, it is generally replaced by an approximate estimate for quasi-regular or irregular sampling (refer to Patil et al. 2024, for more details).

3.2. DPSS or Slepian tapers

Slepian sequences (Slepian 1978), denoted here as $v_k(N, W)$, are also known as Discrete Prolate Spheroidal Sequences (DPSSs). They are specifically designed to minimize spectral leakage outside a user-defined bandwidth W (Thomson 1982). The sequences minimize leakage by concentrating (power) spectral energy at a given frequency f within the frequency range $\{f - W, f + W\}$. The lowest order DPSS taper $k = 0$ results in the most energy concentration within (and the least leakage outside) this range, with higher order tapers having progressively larger leakage. Note that the DPSS tapers are orthonormal, and so the resulting power spectrum estimates are statistically independent and can be averaged. Averaging reduces the variance of the final power spectrum estimate compared to traditional single-taper methods (Thomson 1982).

In practice, selecting the total number of tapers to be $K \lesssim 2NW$ ensures minimal out-of-band(width) leakage, and thereby bias, in the averaged power spectrum estimate. Increasing the time-bandwidth product NW (with N the number of time samples) allows the use of more tapers, thereby reducing the variance of the averaged estimate, but at the cost of decreased frequency

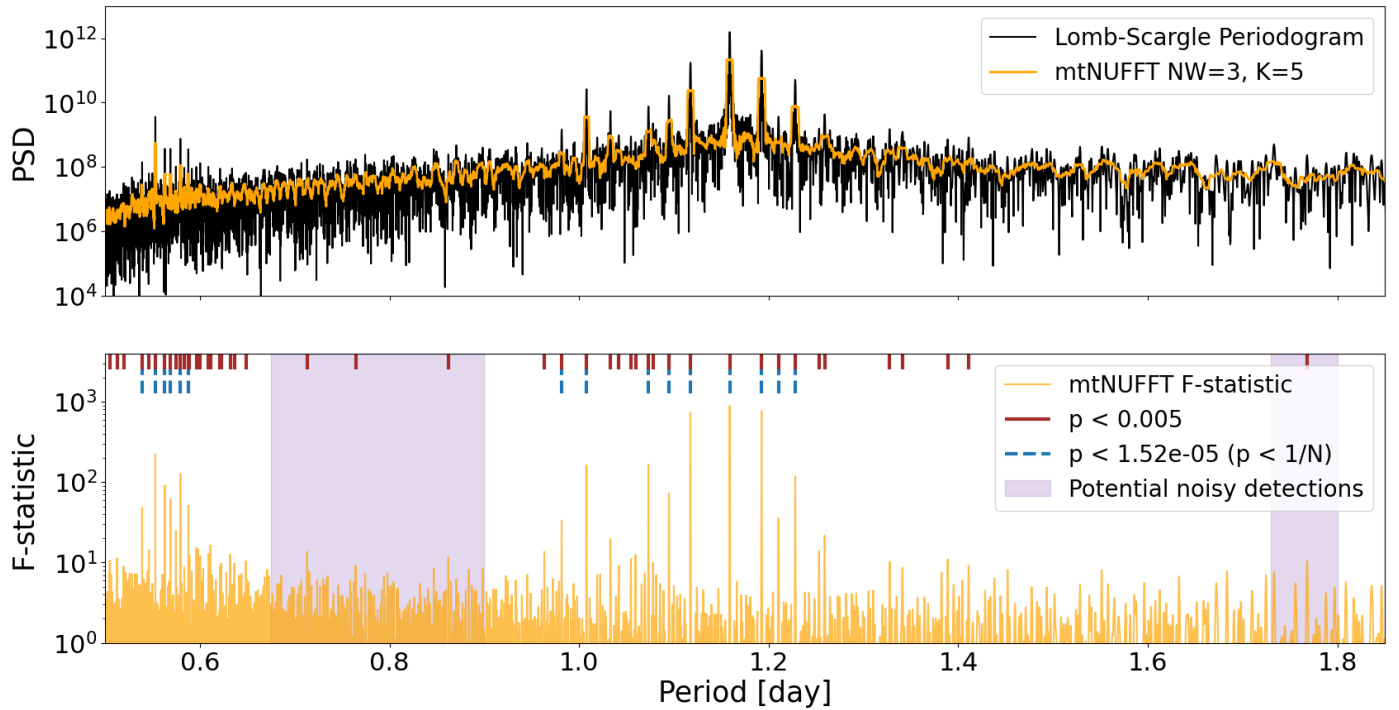


Fig. 1. Comparison of F-test detections for the SPB star KIC7760680 using two significance thresholds, $p < 1/N$ and $p < 10^{-3}$. The lower panel illustrates that adopting the more relaxed threshold of $p < 0.001$ rather than $p < 1/N$ increases sensitivity (yielding 14 additional detections in the figure), but some of these, particularly in the low-power region between 0.4 and 0.5 days, appear noise-like (see Section 3.4).

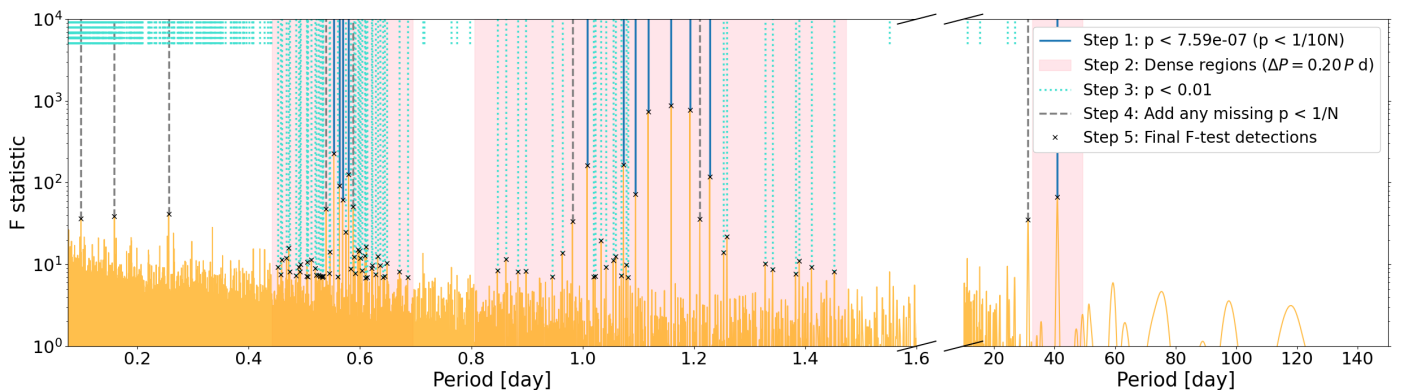


Fig. 2. Illustration of the multi-step procedure to detect g modes in KIC7760680 using the F-test. The five steps are described in Section 3.4.

resolution. The value $NW = 1$ corresponds to the Rayleigh resolution $f_R = 1/T$, whereas $NW > 1$ corresponds to a resolution of $NW \times f_R$ (a rule-of-thumb is to start with $NW = 4$ and tune according to the given problem). We refer the reader to Patil et al. (2024) for more details on the mtNUFFT estimate and ways to choose the parameters NW and K .

3.3. The multitaper F-test

In addition to providing a power spectrum estimate with reduced bias and variance compared to the standard LS periodogram approach, mtNUFFT has the ability to compute an F-statistic, which allows one to test whether the power at a given frequency f is predominantly due to a purely periodic signal or quasi-periodic one (Thomson 1982). Here, a purely periodic signal refers to one having coherent frequency f , amplitude A , and phase ϕ , i.e., a sinusoid $A \cos(2\pi ft + \phi)$. The F-statistic follows an F-distribution

under the null hypothesis that no coherent signal is present at f , and is defined as (Patil et al. 2025)

$$F(f) = \frac{(K-1) |\hat{\mu}(f)|^2 \sum_{k=0}^{K-1} |U_k(N, W; 0)|^2}{\left| \sum_{k=0}^{K-1} y_k(f) - \hat{\mu}(f) U_k(N, W; 0) \right|^2}. \quad (4)$$

Here, $U_k(N, W; 0)$ ¹ represents the Discrete Fourier Transform (DFT) of the k -th order DPSS taper $v_k(N, W)$ at frequency $f = 0$. The term $\hat{\mu}(f)$ is a regression estimate of the complex-valued amplitude of the periodic component at f , defined as

¹ $U_k(N, W)$ is called the discrete prolate spheroidal wave function.

$$\hat{\mu}(f) = \frac{\sum_{k=0}^{K-1} U_k(N, W; 0) y_k(f)}{\sum_{k=0}^{K-1} U_k(N, W; 0)^2}. \quad (5)$$

We then compute the real-valued amplitude of the periodic component at f as

$$A = |\hat{\mu}(f)|^2 \quad (6)$$

and the phase as follows

$$\phi = \arctan \frac{\text{Re}\{\hat{\mu}(f)\}}{\text{Im}\{\hat{\mu}(f)\}}. \quad (7)$$

While Equation 4 defining the F-statistic at frequency f is rather complicated, the idea behind it is simple. One computes $F(f_0)$, the F-statistic at a given frequency f_0 , and evaluates how likely it is to be sampled from an F-distribution with degrees of freedom 2 and $2K-2$. If there is no purely periodic signal present at f_0 (the null hypothesis of the F-test), $F(f_0)$ will follow the F-distribution. To see if $F(f_0)$ is sampled from this distribution, we compute the p-value corresponding to this F-statistic, which represents the probability of obtaining another F-statistic at least as extreme as the one collected. If the p-value is below some threshold α (also called confidence level)², the F-test at frequency f_0 is rejected under the null, that is, we can confidently say that the signal of frequency f_0 in the time-series is purely periodic.

Patil et al. (2025) discuss how one can choose the confidence level α when performing multiple F-tests, one for each frequency $f = \{0, \dots, f_{Nq}\}$. In particular, their approach relies on *selective inference* procedures such as the Benjamini-Hochberg correction for multi-hypothesis testing, which they apply to disentangle exoplanet transit signals from mixed modes in solar-like oscillators. In contrast, the F-test can be even more powerful when dealing with g modes as the majority of these are purely periodic. In the next section, we discuss how we apply the F-test to SPB stars and automatically detect g modes with purely periodic behaviour.

3.4. Multi-step F-test to detect g modes

We know that the multitaper F-test quantifies the degree of strict periodicity in a signal, making it particularly useful for identifying coherent oscillatory modes. In the context of stellar power spectra of SPB stars, such signals ideally correspond to long-lifetime g modes. However, a key challenge lies in selecting the appropriate significance threshold, α , for automatic detection of these modes.

Choosing a conservative threshold (e.g., $\alpha = 0.05$) reduces the rate of false positives but risks missing true g modes, especially those with lower amplitudes. Conversely, a more relaxed threshold increases sensitivity but also admits false positives; periodic signals that are statistically significant yet likely to arise from structured noise rather than physical modes. This issue is particularly pronounced in the low-power regions of the spectrum, where purely periodic noise can mimic the spectral signature (a delta function in the frequency domain) of a g mode and still pass the F-test. Examples of such noisy detections are shown in Fig. 1, which presents the power spectral density (PSD) and the corresponding F-test detections for KIC7760680.

² For example, $p < 0.01$ means that only 1% of the F-statistics under the null hypothesis will be as extreme as the one being tested.

This raises the question: can prior knowledge of g-modes be incorporated to improve detection? A promising approach is to exploit their quasi-uniform period spacing, which causes them to cluster in specific regions of the power spectrum. By combining this structural information with the F-test, we can construct a more robust and targeted detection strategy than relying on the F-test alone, as in Patil et al. (2025). In that work, the presence of purely periodic signals at different frequencies was assessed by repeated F-tests with selective inference (e.g., the Bonferroni and BHq procedures), which limited the set of detectable signals. Here, we relax this restriction by allowing a larger p-value threshold while using the quasi-uniform period spacing of g-modes as prior information to guide the selection of F-test detections.

We visualise this multi-step procedure in Fig. 2 and describe it as follows:

Step 1: $p < 1/M$

First, we compute the eigencoefficients $y_k(f)$ in Equation 3 using the adjoint NUFFT on an interpolated frequency grid of

$$f_i = i/M, \quad i = \{0, 1, \dots\}. \quad (8)$$

Here, interpolation using a zero-padded time-series with resulting length $M = 20N$ ensures that we do not lose a signal between grid points³. We then compute the F-statistic and test the presence of purely periodic signals at each f_i . This results in the testing of multiple hypotheses H_i , which means that we reject the null given a conservative confidence level $\alpha = 1/M$, where M represents the length of the padded time-series.

Step 2: Dense regions given ΔP

In order to automatically detect dense clusters of g modes in the power spectrum, we mark a specified interval around each F-test detection f_0 obtained in step 1. In particular, we choose to mark contiguous dense regions in period space using an interval $P_0 \pm \Delta P \times P_0$, where $P_0 = 1/f_0$. The rationale for this choice is that g modes in SPB pulsators with the same (l, m) values, in non-rotating and young stars (i.e. without dips from mode trapping caused by chemical gradients), exhibit similar period spacings. One can set the value of ΔP based on theoretical or empirical arguments. Here, we choose $\Delta P = 0.2$ days as the approximate upper bound (some 12000 seconds) of typical asymptotic g-mode spacing values $\Delta\Pi_l$ of observed B-type pulsators (Degroote et al. 2010b; Moravveji et al. 2015; Aerts et al. 2019). This scaling is motivated by the typical properties of SPB stars, which exhibit slow pulsations with periods between 0.5 and 5 days (Aerts et al. 2010). The bound $\Delta P \times P_0$ is also adaptive: it ensures that the marked region is narrower at short periods and broader at long periods, reflecting the expected variability timescales.

Step 3: $p < 0.01$ or another chosen threshold

We now find peaks in the entire F-statistic series across frequencies f_i whose p-values are below the threshold $\alpha = 0.01$. This threshold can be modified to change the selectivity of the frequency detection algorithm.

³ The F-test is very sensitive to frequency shifts and thus needs a fine enough frequency grid to detect all purely periodic signals.

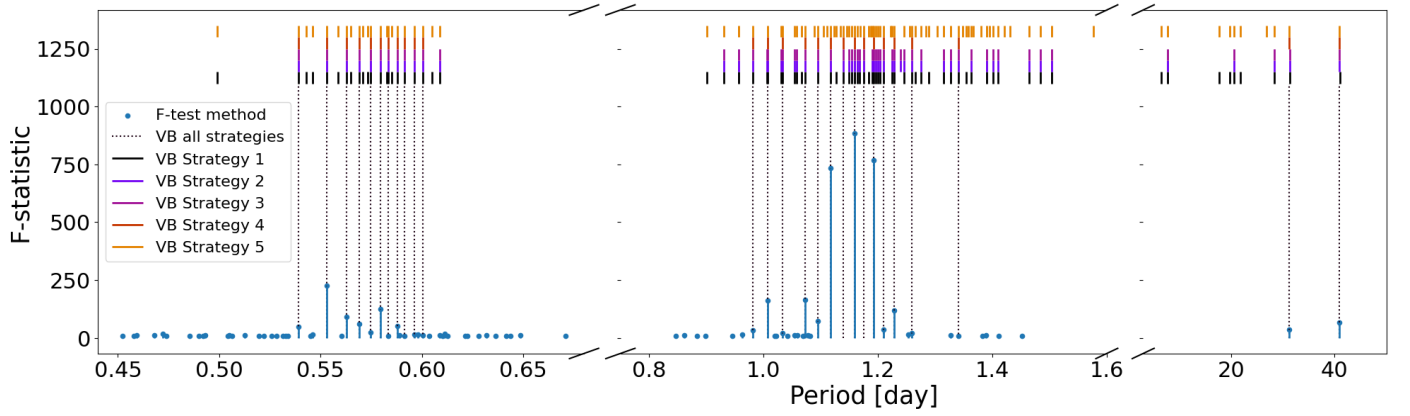


Fig. 3. Frequencies extracted using the multi-step mtNUFFT/F-test and their comparison with estimates in VB21 for the SPB KIC7760680. The comparison is made with frequencies extracted by each of the five prewhitening strategies, as well as those consistent across all strategies (dotted grey lines). Values of $NW = 4$ and $K = 7$ with a p-value $p < 0.01$ were used.

Table 1. Frequency matches between the periodic g-mode signals detected by the F-test ($NW = 4$, $K = 7$, $p < 0.01$) and those reported using Strategy 3 in VB21 for KIC7760680. Matches are defined when the frequencies agree within 3σ (or 6σ if highlighted in purple). The signals are listed in order of increasing frequency. For each frequency \hat{f}_0 , we report the corresponding amplitude A , phase ϕ , jackknife uncertainties on the frequency, amplitude, and phase $\sigma_{\hat{f}_0}$, $\sigma_{\hat{A}}$, $\sigma_{\hat{\phi}}$ and the F-statistic [columns under ‘Patil et al. (this paper)’]. The corresponding values from VB21 are shown in the adjacent columns. The Nonlinear ID column from VB21 indicates the order in which each independent frequency was extracted during the prewhitening procedure. If a signal was identified as a combination frequency, this column lists the corresponding combination of independent frequencies, which may indicate a nonlinear resonant mode (see VB21).

Patil et al. (this paper)							VB21 Strategy 3						
Frequency \hat{f}_0 (1/day)	$\sigma_{\hat{f}_0}$ (1/day)	Amplitude \hat{A} (ppm)	$\sigma_{\hat{A}}$ (ppm)	Phase $\hat{\phi}$ (rad)	$\sigma_{\hat{\phi}}$ (rad)	F-statistic	Frequency \hat{f}_0 (1/day)	$\sigma_{\hat{f}_0}$ (1/day)	Amplitude \hat{A} (ppm)	$\sigma_{\hat{A}}$ (ppm)	Phase $\hat{\phi}$ (rad)	$\sigma_{\hat{\phi}}$ (rad)	Nonlinear ID
0.024414	0.000041	181.073034	5.222283	0.170401	0.118590	66.399528	0.024408	0.000026	201.337980	14.076463	1.623552	0.069915	freq_1 - freq_2
0.031997	0.000077	166.228713	6.642989	1.879346	0.119531	35.294917	0.031968	0.000031	168.803104	14.076463	2.985211	0.083390	freq_3 - freq_1
0.708723	0.000068	206.558042	2.788264	1.544018	0.026121	9.188898	0.709102	0.000044	120.270005	14.076463	-0.536887	0.117041	freq_24 - freq_5
0.719978	0.000067	212.459463	45.382386	-2.885599	0.094390	10.976999	0.719421	0.000073	72.770917	14.076463	2.871236	0.193435	freq_46
0.745616	0.000017	307.311704	8.517915	2.395007	0.121733	8.657512	0.745761	0.000015	354.643486	14.076463	-1.400792	0.039692	freq_11
0.753164	0.000117	287.157437	2.855840	0.287936	0.114001	10.234381	0.753171	0.000044	121.105066	14.076463	1.690412	0.116233	freq_26
0.794206	0.000052	533.514136	29.953011	-0.981846	0.127727	21.701908	0.794263	0.000011	463.265803	14.076463	-0.782122	0.030385	freq_9
0.814302	0.000003	1773.909360	58.448621	2.262334	0.004290	118.497266	0.814310	0.000003	1742.943213	14.076463	-0.826346	0.008076	freq_4
0.826203	0.000045	467.395425	34.159221	1.798332	0.112823	35.698434	0.826299	0.000021	246.865471	14.076463	-0.831270	0.057021	freq_13
0.838546	0.000003	4994.183939	59.291025	-0.689480	0.000635	767.373999	0.838526	0.000001	5051.359257	14.076463	-0.759907	0.002787	freq_2
0.862858	0.000003	9723.284972	37.756610	-1.131417	0.001833	883.618296	0.862876	0.000001	9861.385107	14.076463	2.617689	0.001427	freq_1
0.894855	0.000029	3224.571614	46.625277	-2.811816	0.083097	733.948659	0.894848	0.000002	3411.811513	14.076463	1.198383	0.004126	freq_3
0.913386	0.000029	1029.591640	31.683735	-1.504075	0.083445	72.418387	0.913385	0.000006	945.192152	14.076463	3.106222	0.014893	freq_6
0.931782	0.000038	715.868768	15.866187	1.169553	0.118725	165.600997	0.931822	0.000009	618.398057	14.076463	-2.891580	0.022763	freq_7
0.948103	0.001233	200.405627	11.312159	-2.771724	0.129250	11.146117	0.948578	0.000071	74.589479	14.076463	-1.225614	0.188719	freq_10 - freq_39
0.967961	0.000052	553.234919	11.769183	-0.617589	0.125204	19.687436	0.967846	0.000010	543.280547	14.076463	-0.329278	0.025910	freq_8
0.992171	0.000029	1223.301000	23.308126	1.393588	0.092141	162.323962	0.992183	0.000004	1391.618410	14.076463	-2.969371	0.010115	freq_5
1.018693	0.000081	310.666752	9.471978	-0.424294	0.120711	33.368551	1.018649	0.000024	219.803346	14.076463	-0.963861	0.064041	freq_16
1.642273	0.000111	75.988482	2.628093	1.081864	0.106613	12.795054	1.642385	0.000110	48.059778	14.076463	0.204618	0.292895	freq_13 + freq_19
1.665803	0.000808	87.815637	13.853889	1.895834	0.118510	11.999618	1.665832	0.000074	71.062001	14.076463	-0.668319	0.198087	freq_1 + freq_27
1.677092	0.000105	80.604648	4.974847	-0.502215	0.096165	15.194213	1.677221	0.000090	58.473812	14.076463	1.498597	0.240731	freq_1 + freq_4
1.690659	0.000034	73.816269	10.001070	-2.120619	0.020230	7.708872	1.690679	0.000101	52.427522	14.076463	0.524468	0.268494	freq_11 + freq_52
1.701336	0.000045	151.914070	2.984866	-2.413831	0.113666	50.981831	1.701408	0.000041	130.015238	14.076463	0.670278	0.108268	freq_1 + freq_2
1.713849	0.000079	73.420379	1.597691	-1.610655	0.026821	8.764348	1.713733	0.000075	70.503079	14.076463	0.387284	0.199657	freq_1 + freq_12
1.725750	0.000029	211.006785	1.792547	0.480859	0.092016	125.895839	1.725747	0.000022	244.434095	14.076463	-2.108996	0.057588	2 * freq_1
1.740031	0.000073	77.773098	5.179423	-0.614312	0.090580	24.791359	1.740075	0.000057	92.246351	14.076463	-1.039813	0.152596	freq_1 + freq_15
1.757712	0.000038	150.079003	4.566146	1.817308	0.106027	61.217982	1.757737	0.000039	135.221683	14.076463	2.655345	0.104099	freq_1 + freq_3
1.776312	0.000029	151.863889	3.144222	-2.831968	0.091919	91.577278	1.776275	0.000038	139.223832	14.076463	-1.692613	0.101107	freq_1 + freq_6
1.808309	0.000029	473.315500	13.365018	-1.343183	0.082974	225.384487	1.808310	0.000011	463.596624	14.076463	-0.271033	0.030364	freq_3 + freq_6
1.855029	0.000029	93.273912	6.475357	-0.241015	0.078317	47.669494	1.855055	0.000058	90.752392	14.076463	-1.479945	0.155108	freq_1 + freq_5

Notes. Frequencies are considered matched if $|\hat{f}_{0,\text{Patil}} - \hat{f}_{0,\text{VB21}}| \leq 3\sigma_{\text{Patil+VB21}}$ where $\sigma_{\text{Patil+VB21}} = \sqrt{\sigma_{\hat{f}_0,\text{Patil}}^2 + \sigma_{\hat{f}_0,\text{VB21}}^2}$. The ones highlighted in purple are the ones that match within $6\sigma_{\text{Patil+VB21}}$ but are within 0.00072 d^{-1} (the Rayleigh resolution f_R).

Step 4: $p < 1/N$: In order to ensure that we do not miss any significant frequencies that do not necessarily lie in a dense region, we select frequencies whose p-value are below the threshold $p < 1/N$. Thomson (1982) suggests using $p < 1/N$ as a rule of thumb to ensure that the F-test detections are significant.

Step 5: Final F-test detections

In the final step, we generate the list of frequencies detected by this procedure. This list includes frequencies whose F-tests were rejected under the null in Step 1, as

well as frequencies detected in Step 3 that belong to any of the dense regions estimated in Step 2, and any significant missing frequencies that were selected in Step 4.

4. Results

In Section 4.1, we compare, frequency by frequency, the F-test method proposed in this work with those of VB21. We also examine how variations in multitaper parameters and p-values af-

Table 2. Number of periodic g-mode signals reported by VB21 (column ‘VB21, Strategy 3’) compared with those detected by the F-test (column ‘F-test, this paper’) for the sample of SPB stars analysed here (column ‘KIC’). The total number of VB21 detections (T_{VB}) is further divided into independent (I_{VB}) and combination frequencies (C_{VB} , i.e., potential nonlinear modes), following their classification. Performance of the F-test is evaluated by varying the multitaper parameters NW , K , and significance threshold p (columns $NW = 4, K = 7; NW = 3, K = 5; p < 0.005$; and $p < 0.01$). For each configuration, we report the total number of detections (‘Total’ T) and the number of 3σ matches with VB21 (‘Match’). The matches are separated into independent (I_m) and combination (C_m) frequencies, with $T_m = I_m + C_m$.

KIC	Number of g-mode detections																		
	VB21, Strategy 3			F-test, this paper															
				NW = 4, K = 7						NW = 3, K = 5									
				p < 0.005			p < 0.01			p < 0.005			p < 0.01						
Total T_{VB}	Independent I_{VB}	Combination C_{VB}	Total T	T_m	I_m	C_m	Total T	T_m	I_m	C_m	Total T	T_m	I_m	C_m	Total T	T_m	I_m	C_m	
3240411	178	37	141	419	72	29	43	640	81	30	51	344	64	31	33	558	78	31	47
3459297	180	42	138	159	43	26	17	278	45	26	19	84	32	19	13	134	39	20	19
3756031	182	26	156	206	89	22	67	266	96	23	73	92	50	20	30	123	62	21	41
3839930	190	25	165	113	46	16	30	170	56	16	40	118	39	13	26	175	42	13	29
3865742	190	12	178	200	49	8	41	329	58	8	50	98	37	7	30	142	43	7	36
4930889	175	24	151	228	44	17	27	376	46	17	29	111	35	14	21	154	41	14	27
4936089	181	29	152	131	29	18	11	219	30	18	12	220	19	16	3	350	25	16	9
4939281**	144	28	116	109	8	6	2	175	8	6	2	5	2	2	0	5	2	2	0
5084439*	183	17	166	32	11	3	8	49	13	3	10	45	12	2	10	63	16	3	13
5309849	190	34	156	259	80	28	52	389	90	28	62	193	66	26	40	291	75	26	49
5941844	184	23	161	537	64	18	46	858	75	18	57	141	60	16	44	192	72	17	55
6352430	191	38	153	193	55	27	28	299	70	29	41	207	51	27	24	313	58	27	31
6462033	191	37	154	474	124	32	92	686	131	32	99	463	116	30	86	704	124	30	94
6780397	181	23	158	237	47	15	32	374	51	16	35	106	39	13	26	150	44	14	30
7630417	179	50	129	426	78	34	44	620	85	36	49	260	32	11	21	440	33	11	22
7760680	65	22	43	56	29	14	15	87	30	14	16	52	24	11	13	77	28	13	15
8057661	191	48	143	384	62	26	36	629	69	28	41	469	80	36	44	714	82	36	46
8087269	162	20	142	86	38	16	22	150	49	16	33	94	37	17	20	139	43	17	26
8255796	186	22	164	87	67	20	47	102	72	21	51	50	32	14	18	57	36	14	22
8324482	192	34	158	359	121	31	90	497	128	31	97	290	118	30	88	392	126	31	95
8381949	183	32	151	628	42	21	21	980	43	21	22	640	34	18	16	1032	36	19	17
8459899	178	24	154	133	67	21	46	183	73	21	52	73	50	17	33	87	55	18	37
8714886	189	33	156	229	76	28	48	323	83	28	55	388	81	30	51	594	82	30	52
8766405	160	18	142	211	48	12	36	300	55	12	43	193	45	11	34	325	48	11	37
9020774	190	26	164	206	36	17	19	358	42	19	23	137	22	13	9	223	27	14	13
9227988	174	16	158	48	37	14	23	63	42	14	28	229	39	13	26	355	45	13	32
9715425**	55	3	52	3	1	1	0	3	1	1	0	1	0	0	0	1	0	0	0
9964614	187	38	149	302	59	19	40	460	62	20	42	153	18	8	10	228	18	8	10
10220209*	186	34	152	1	1	0	1	1	1	0	1	21	7	2	5	32	11	4	7
10285114	165	48	117	130	32	18	14	230	35	19	16	89	17	10	7	158	17	10	7
10526294	78	30	48	83	25	11	14	122	28	13	15	51	34	21	13	69	38	22	16
10536147	190	36	154	105	49	21	28	130	51	22	29	90	37	15	22	132	44	18	26
10658302	172	28	144	137	67	23	44	198	79	24	55	139	54	21	33	209	63	21	42
11152422	167	27	140	94	43	12	31	140	49	12	37	74	28	10	18	100	31	10	21
11360704	176	21	155	114	17	4	13	186	26	5	21	23	4	2	2	39	5	2	3
11454304	179	43	136	285	75	29	46	404	83	32	51	304	62	22	40	457	73	27	46
11971405	175	13	162	35	19	5	14	50	22	5	17	32	12	4	8	47	14	4	10
12258330	189	36	153	482	102	31	71	746	110	31	79	530	87	30	57	857	98	31	67

Notes. The ‘Total’ T column showing F-test detections for $NW = 4, K = 7$ and $p < 0.01$ is highlighted in grey as it consistently works well. The horizontal highlights refer to the categories of *large gaps in time-series and **outbursting stars, with the former classification defined in this paper and the latter following VB21 (see their Table 3).

fect our F-test detections. Finally, we compare the period spacings derived from our mode detections with those reported by PD21, highlighting additional spacings and dips that may prove valuable for future new inferences and insights into the internal structure of SPB stars.

4.1. Comparison with Van Beeck et al. (2021)

We compare the mode frequencies extracted using our mtNUFFT/F-test multi-step procedure (see Section 3.4) with those in VB21. They implement five distinct prewhitening strategies to investigate how mode frequency estimates are affected by (1) the choice of initial parameters for the optimization (i.e., parameter hinting), (2) the stopping criteria, and (3) whether parameter optimization at the end of each iterative step is per-

formed using linear or nonlinear least-squares regression. Instead of iteratively extracting and optimizing the mode frequencies, we estimate them in one iteration based on two criteria

1. NW and K for computing the mtNUFFT F-statistic, which is then tested against the F distribution;
2. The p-value threshold α : $p < \alpha$.

In Figure 3, we compare our approach given multitaper parameters $NW = 4, K = 7$ and $p < 0.001$ with the VB21 strategies for the SPB star KIC7760680. We see that the frequencies consistently found across all five strategies in VB21, that is, those that lie within 3σ uncertainties, also coincide with those from the F-test detections. This suggests that the F-test extracts at least those mode frequencies that are in the most conservative VB21 strategy 4, a hypothesis we have verified for all 38 SPBs in our sample. In addition, some of the signals we detect coincide with

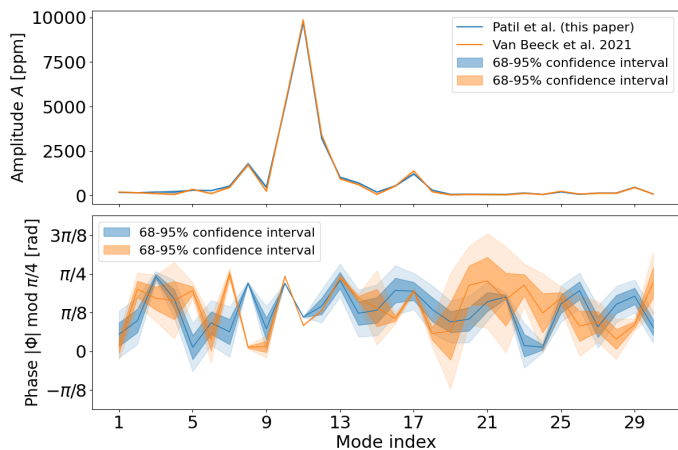


Fig. 4. Amplitude and phase comparison of g modes estimated using the F-test procedure described in this paper and those computed in VB21 using Strategy 3 for KIC7760680. The comparison includes modes in our F-test catalogue that have a 3σ (or 6σ) match with those reported by VB21. To highlight relative shifts unambiguously, phase differences are shown as absolute values, mapped modulo $\pi/4$. The 68% and 98% confidence intervals are indicated by dark and light shaded regions, respectively, and are computed using the jackknife uncertainty estimates of amplitude and phase. The corresponding amplitude, phase, and uncertainty values are listed in Table 1. Note that although the amplitude plot includes the confidence intervals, they are too small to be visible.

the ones solely detected by strategies 1, 2, 3, as well as some that are undetected by each of the strategies. These frequencies could potentially be new independent modes, manifestations of rotationally-split modes, or combinations of modes that retain their purely periodic behaviour. We also emphasize that any frequency in VB21 not picked up by the F-test could hint at a damped nature for those g-modes; the modes potentially have quasi-periodic behaviour that the F-test discards.

We now quantitatively estimate how many of our multi-step F-test mode detections match the estimates in VB21. We compare our results for the frequency values specifically with Strategy 3 in VB21. This strategy chooses the highest amplitude peak in the (residual) LS periodogram at each iterative prewhitening step using a likelihood ratio test and then performs a nonlinear least-squares optimization to achieve the final frequency value. We compare with this strategy since it performs best for 34 out of the 38 pulsators used in this study. Note that VB21 uses a Bayesian information criterion (BIC) to evaluate whether the frequency extracted in an iteration should be included in the nested regression model. This evaluation is in the form of a p-value for the likelihood ratio test $p_{LRT} > 0.05$.

Table 1 shows the frequency-by-frequency comparison between our approach and VB21 Strategy 3 for KIC7760680. We use $NW = 4$, $K = 7$ and $p < 0.01$ as mentioned above. The frequency grid step in our mtNUFFT/F-test estimate after padding to a length of $M = 20N$ is $0.05f_R$ (where $f_R \equiv 1/T$ or $1/N$ is the Rayleigh resolution). This is smaller than the grid step used in VB21, which is about $0.1 f_R$. However, the frequencies we choose upon applying the multi-step F-test procedure have a minimum separation of $0.0018 d^{-1}$ (or $2.5f_R$) similar to VB21 and 3σ uncertainties of both approaches are used to find matches. Our approach detects a total of 114 frequencies, which is approximately twice the number extracted by VB21. Among the 65 frequencies reported by VB21, 25 are found to match those identified in our analysis. Since some of the frequencies with the highest F-statistics were not included within the 3σ

matching criterion, we relaxed the threshold to 6σ uncertainties for both approaches (while still enforcing the f_R resolution limit). This adjustment yielded five additional matches, which are highlighted in purple in the table. These frequencies exhibit very small jackknife uncertainties owing to their high F-statistics and precise frequency estimates, which explains why their deviations exceed the 3σ limit.

In addition to the frequency estimates, Table 1 lists the $1-\sigma$ uncertainty on the estimates, which is computed using the jackknife estimator as described in Patil et al. (2025). Specifically, the uncertainties are obtained by sequentially omitting one DPSS taper v_k (i.e., removing a single eigencoefficient $y_k(f)$ at a time) and evaluating the resulting variability in the frequency detections, which provides an estimate of the variance and hence the standard deviation σ of the F-test frequencies. The procedure is detailed below:

1. Compute the delete-one F-statistic $F_{\setminus j}(f)$ by omitting the eigencoefficient $y_j(f)$ and the corresponding wave function $U_j(N, W; 0)$ from Equations (4) and (5);
2. Obtain delete-one F-test detections $\hat{f}_{0,\setminus j}$ by applying a threshold $p < \alpha$ to each of the delete-one F-statistic estimates $F_{\setminus j}(f)$;
3. Estimate the jackknife variance of the detection \hat{f}_0 as

$$\widehat{\text{Var}}_J\{\hat{f}_0\} = \frac{K-1}{K} \sum_{j=0}^{K-1} [\hat{f}_{0,\setminus j} - \hat{f}_{0,\setminus \bullet}]^2, \quad (9)$$

where $\hat{f}_{0,\setminus \bullet}$ is the average of $\hat{f}_{0,\setminus j}$. Our jackknifed uncertainty estimates are then given by $\sigma_{\hat{f}_0} = \sqrt{\widehat{\text{Var}}_J\{\hat{f}_0\}}$. Equation 12 in Patil et al. (2025) provides an analytical expression for the variance, $\text{Var}\{\hat{f}_0\}$, of a periodic signal frequency estimate. This variance is typically a few percent larger than the Cramér–Rao bound (Rife & Boorstyn 1976; Thomson 2007), which represents the theoretical minimum variance achievable. Consequently, the analytical expression serves as a practical upper bound on frequency precision. We use it to validate our jackknife variance estimates, which turn out to be roughly consistent with the VB21 estimates. Seven of our 26 frequency uncertainties σ_f (27%) in Table 1 are smaller than those reported in VB21, and the rest are within an order of magnitude. This shows that we do not lose much frequency precision when working in the frequency domain using the F-test, and any resolution lost in the power spectrum due to tapering is recovered by the F-test.

Table 1 also lists the F-statistic, amplitude A and phase ϕ estimates for each frequency, computed using Equations 6 and 7), as well as the jackknife uncertainties on amplitude $\sigma_{\hat{A}}$ and phase $\sigma_{\hat{\phi}}$ [refer to Equation (9)]. To validate our results, we compare our amplitude estimates with those from VB21 in Fig. 4, finding excellent agreement. The phase estimates (ϕ) show larger deviations from those of VB21, but generally remain within the 95% confidence interval.

We note that the phase of a multiperiodic harmonic signal is inherently challenging to estimate. Our method employs a one-step FFT-based estimation of ϕ , in contrast to the iterative time-domain prewhitening approach used by VB21. Finally, Table 1 also includes the independent and combination frequency labels given by VB21 for their frequencies. Our approach matches 14 of the independent and 16 of the combination frequencies reported by VB21.

We perform such extraction for each of the 38 stars, the results of which are summarized in Table 2. The total number of g-mode detections using our methodology (T) are compared with

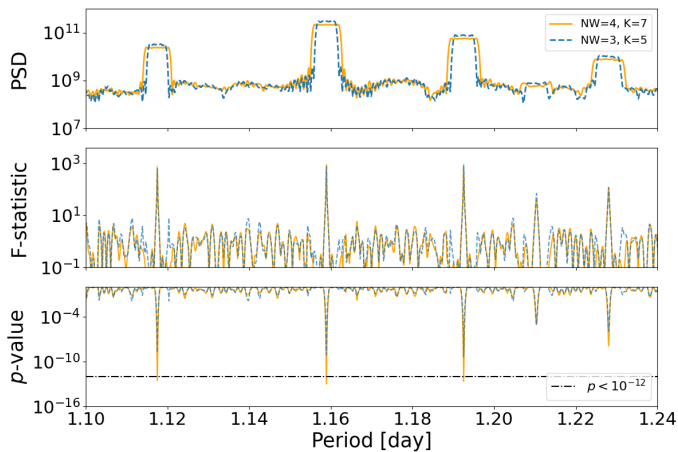


Fig. 5. Effect of changing the time–bandwidth product NW and number of tapers K from $NW = 4, K = 7$ (orange) to $NW = 3, K = 5$ (blue) for KIC7760680. The top panel shows the mtNUFFT periodograms, while the middle and bottom panels display the corresponding F-statistics and p-values. The bottom panel also includes a $p < 10^{-12}$ threshold, highlighting that $NW = 4$ yields three detections, whereas $NW = 3$ produces none.

the total number of detections T_{VB} in VB21, which is equal to $T_{VB} = I_{VB} + C_{VB}$ (VB21 distinguishes between independent and combination frequencies in their frequency detection algorithm). We then find 3σ matches between our mode frequencies and those in VB21 to compute the matching frequencies T_m . These matches frequencies are divided into independent and combination frequencies depending on the non-linear label of the matching frequency in VB21 $T_m = I_m + C_m$.

We perform this extraction for each of the 38 stars, and the results are summarized in Table 2. For each star, we compare the total number of g-mode detections obtained with our methodology (T) to the total number of detections reported by VB21, denoted as T_{VB} . Note that VB21 distinguishes between independent (I_{VB}) and combination (C_{VB}) frequencies in their detection algorithm, such that $T_{VB} = I_{VB} + C_{VB}$. These quantities are listed in the table. We then identify 3σ matches between our detected mode frequencies and those reported by VB21, computing the number of matching frequencies T_m for each star. The matched frequencies are further divided into independent and combination frequencies based on the non-linear ID (refer to Table 1) of the corresponding frequency in VB21, such that $T_m = I_m + C_m$.

In blue, we highlight the results using $NW = 4, K = 7$ and $p < 0.01$, which are the same as those shown in Figure 3 and Table 1 for KIC7760680. To show how our results vary based on the choice of NW, K and the p-value, we include overall results for different multitaper bandwidths $NW = 3$ and $NW = 4$ (and thereby the number of tapers $K = 2NW - 1$) and for different p-values, $p < 0.01$ and $p < 0.005$.

Table 2 shows that, for a fixed significance threshold of e.g., $p < 0.005$, the number of detections usually (but not always) decreases as the time–bandwidth product NW is reduced. Conversely, when NW is held constant, the number of detections decreases with smaller p-values, reflecting the more conservative nature of stricter thresholds.

Figure 5 illustrates the effect of changing multitaper (mtNUFFT) parameters from $NW = 4, K = 7$ (orange) to $NW = 3, K = 5$ (blue) for KIC7760680. While both settings recover the same g modes, reducing NW leads to larger p-values, reflecting reduced robustness of the F-test. At the same time, the narrower spectral concentration with $NW = 3$ produces slightly sharper

PSD peaks, whereas the higher NW smooths the spectrum but yields more statistically significant detections.

Increasing NW , and consequently K , enhances the robustness of the multitaper F-test against noise, but it reduces the ability to resolve closely spaced periodic signals. In theoretical terms, this increases the degrees of freedom, $2K - 2$, of the denominator (noise term) in the variance ratio defining F-statistic (see Equation 4). For SPB stars with sparse power spectra containing only a few isolated g modes, choosing a moderate-to-large NW improves detection reliability. Conversely, for dense spectra with many closely spaced modes (e.g., KIC 3240411), a smaller NW is preferable to preserve frequency resolution, even if this comes at the cost of higher variance.

Additionally, for stars such as KIC5084439 and KIC10220209, using $NW = 3$ and $K = 5$ produces better results, likely because these stars contain large gaps in their time series, leading to poorly resolved modes in the data. KIC5084439 has a gap of approximately 190 days, covering more than a quarter of the total time-series length, while KIC10220209 has four gaps of roughly 100 days each, with the largest spanning about 280 days, corresponding to one-fifth of the total time-series duration. Such gaps are considered large because they significantly reduce the effective duty cycle of the observations, thereby decreasing the frequency resolution and introducing strong windowing effects. In other words, the smaller number of available samples, N , results in a larger effective bandwidth, W , for a given time–bandwidth product, NW . To increase the number of detections for such stars, one could consider using a smaller NW together with a less conservative p-value threshold.

We also note that KIC4939281 and KIC9715425 are outbursting stars. These outbursting stars are defined in VB21 as those that display outburst-like features in their light curves, characterized by significant deviations from the baseline brightness, which remain visible in the residual light curve after prewhitening. Because the F-test is sensitive to small frequency shifts (or any deviations from strict periodicity), it likely identifies only a limited number of modes in these outbursting cases. Aside from these special instances, $NW = 4, K = 7$ with $p < 0.01$ yields consistently reliable results across most stars.

Figure 6 shows the percentage of g-mode matches between our method and Strategy 3 for the 19 SPBs classified as High- f_{sv} in VB21. These stars are characterized by high SNRs in their frequency spectra and, correspondingly, a high f_{sv} : a metric quantifying how well the regression models (after prewhitening) describe the light curve of a star. We observe that on average, a higher percentage of independent mode frequencies in VB21 have matches with our F-test detections as opposed to combination frequencies. In addition, the percentages are not functions of the rotation frequencies of the stars (see bottom panel of Figure 6), i.e., there appears to be no dependence on stellar rotation. Instead, the percentages appear to depend on mode density in the power spectrum, since combination frequencies are more likely to occur in mode-dense regions. The independent versus combination mode trend is also seen in SPB stars labelled as Low- f_{sv} as seen in Figure 7, which include high mode density and outbursting stars.

Note that some stars, e.g., KIC10220209 and KIC5084439 in Figure 6, and KIC4939281 and KIC9715425 in Figure 7, show very few detections of g-modes (see also Table 2). These stars fall into the categories of having large gaps in their time series or being outbursting stars. For such cases, additional modes can be recovered by adopting a less conservative p-value threshold

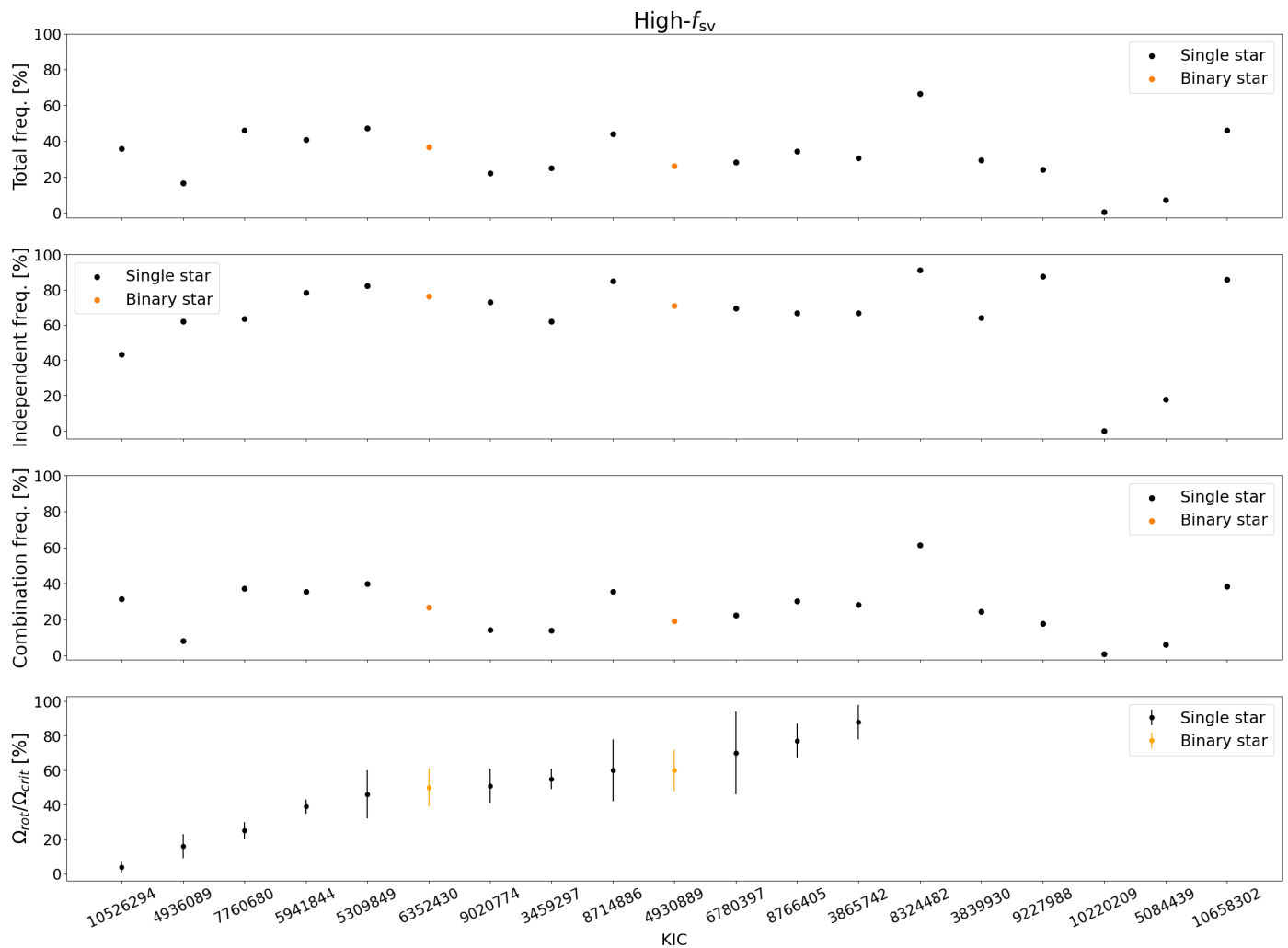


Fig. 6. Comparison of our approach with VB21 (Strategy 3) for SPBs identified as High- f_{sv} stars. The top and middle panels show the percentage of matched frequencies (total, independent, and combination). The bottom panel illustrates the near-core rotation frequency Ω_{rot} relative to the star’s critical rotation frequency Ω_{crit} deduced by PD21. In this panel, we see that the match percentage does not seem to have dependence on the rotation frequency. Single and binary stars (Pápics et al. 2013, 2017) are shown in black and orange, respectively. More of the stars might be binaries, but two of them are confirmed. Also, for some stars we do not have an estimate of the (near-core) stellar rotation frequency.

for the F-test, as demonstrated for KIC9715425 in Figure A.18 in Appendix A.

The overall match percentage are similar for High- f_{sv} and Low- f_{sv} stars. These percentages are shown in Figure 8. We see that the Low- f_{sv} and outbursting stars (as defined in VB21), which have beating cycles that are not well covered by the 4-year Kepler light curves, have fewer mode frequency matches. The SPB stars revealing high mode density in the definition of VB21 have the highest matching percentages between the two frequency analysis methods.

4.2. Comparison with Pedersen et al. (2021)

We next examine whether our method can recover the frequencies typically used for asteroseismic modelling from period spacing patterns. For this, we compare our results with those of PD21, who analyzed 26 of the 38 SPB stars in our sample using Strategy 1 from VB21. Unlike the VB21 approach, PD21 did not impose a limit of 200 significant frequencies but extended their prewhitening analysis to all signals with amplitudes exceeding an SNR threshold of 4.0. In addition, they interpret the frequencies with the purpose of asteroseismic modelling. This requires

one to obtain period spacing patterns for mode identification and derivation of the internal rotation frequency. Since VB21’s Strategy 1 (which is used in PD21) is known to be less performant than Strategy 3, we do not perform a frequency-by-frequency comparison with PD21 (as in Section 4.1). Instead, we directly compare the period spacing patterns present in our F-test mode detections with those suggested by PD21.

To compare our detected period-spacing patterns with those reported by PD21, we identify matching modes using the criteria in Table 1: frequency agreement within the Rayleigh limit and within 3σ uncertainties, accounting for precision differences from the F-test and prewhitening. Figure 9 shows the resulting comparison for KIC7760680. The mtNNUFFT spectrum and corresponding F-statistic reveal modes consistent with the primary period-spacing pattern of PD21. Matched detections are plotted as orange diamonds along the PD21 sequence, while additional orange points mark secondary ΔP sequences derived from consecutive unmatched detections as well as nearby PD21 modes. PD21 modes are only included in these secondary sequences if they lie adjacent (beyond the 3σ match threshold) to one of our unmatched g modes. A potential secondary pattern

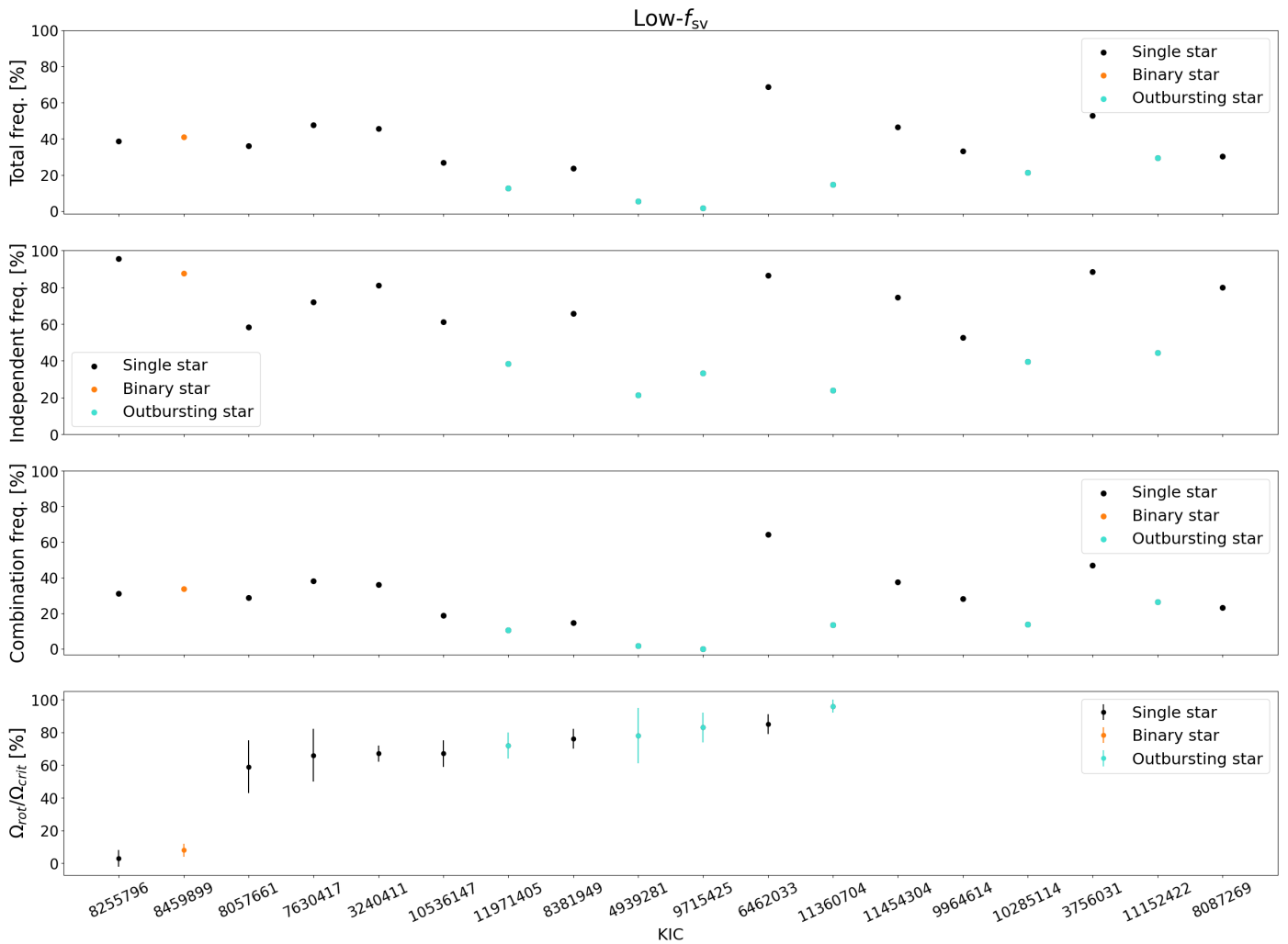


Fig. 7. Same as Figure 6 but for the Low- f_{sv} stars. KIC8459899 is marked in orange as it is suspected to be a binary star (Lehmann et al. 2011).

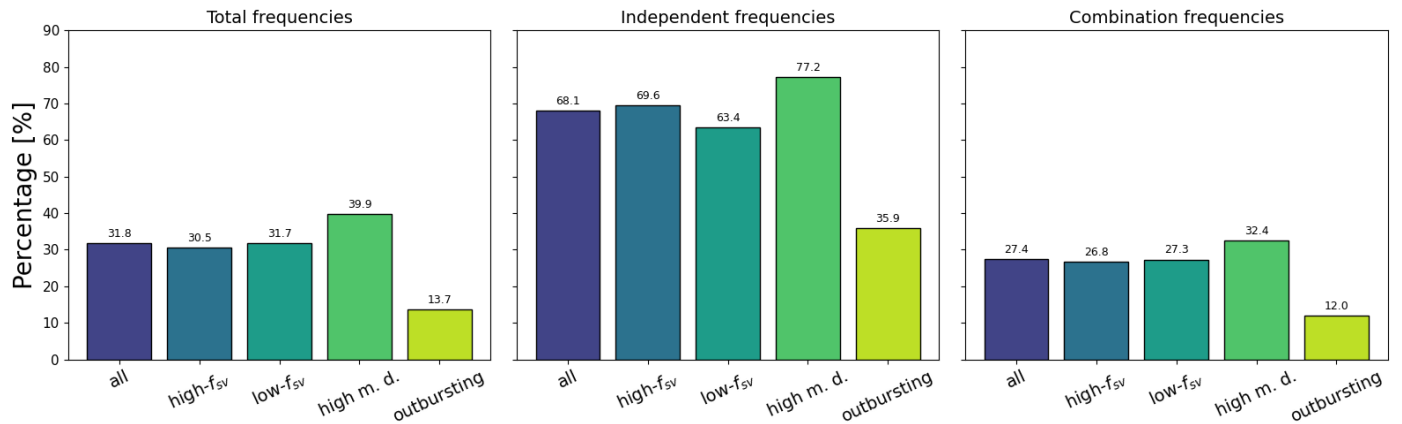


Fig. 8. Match percentage between our F-test detections given $NW = 4$, $K = 7$ and $p < 0.1$ and VB21, Strategy 3. The left, middle, and right panels show the percentage of total, independent, and combination matched frequencies, respectively. We consider the sub-classes among the SPB stars defined by VB21, to which we refer for their detailed definitions.

(brown) is also automatically identified from modes lying below the primary sequence.

KIC7760680 serves as a benchmark SPB star, exhibiting the longest observed sequence of consecutive dipole $l = 1$ g modes in radial order n (with additional frequencies interspersed). The period-spacing pattern of these modes clearly shows the com-

binated effects of rotation and near-core chemical mixing (as reported by Pápics et al. (2015)). Owing to its extensive previous asteroseismic modelling (Moravceji et al. 2016; Michielsen et al. 2021), this star provides an ideal test case for assessing our frequency-detection method's ability to recover period-spacing patterns. As shown in Figure 9, we recover most of the g modes

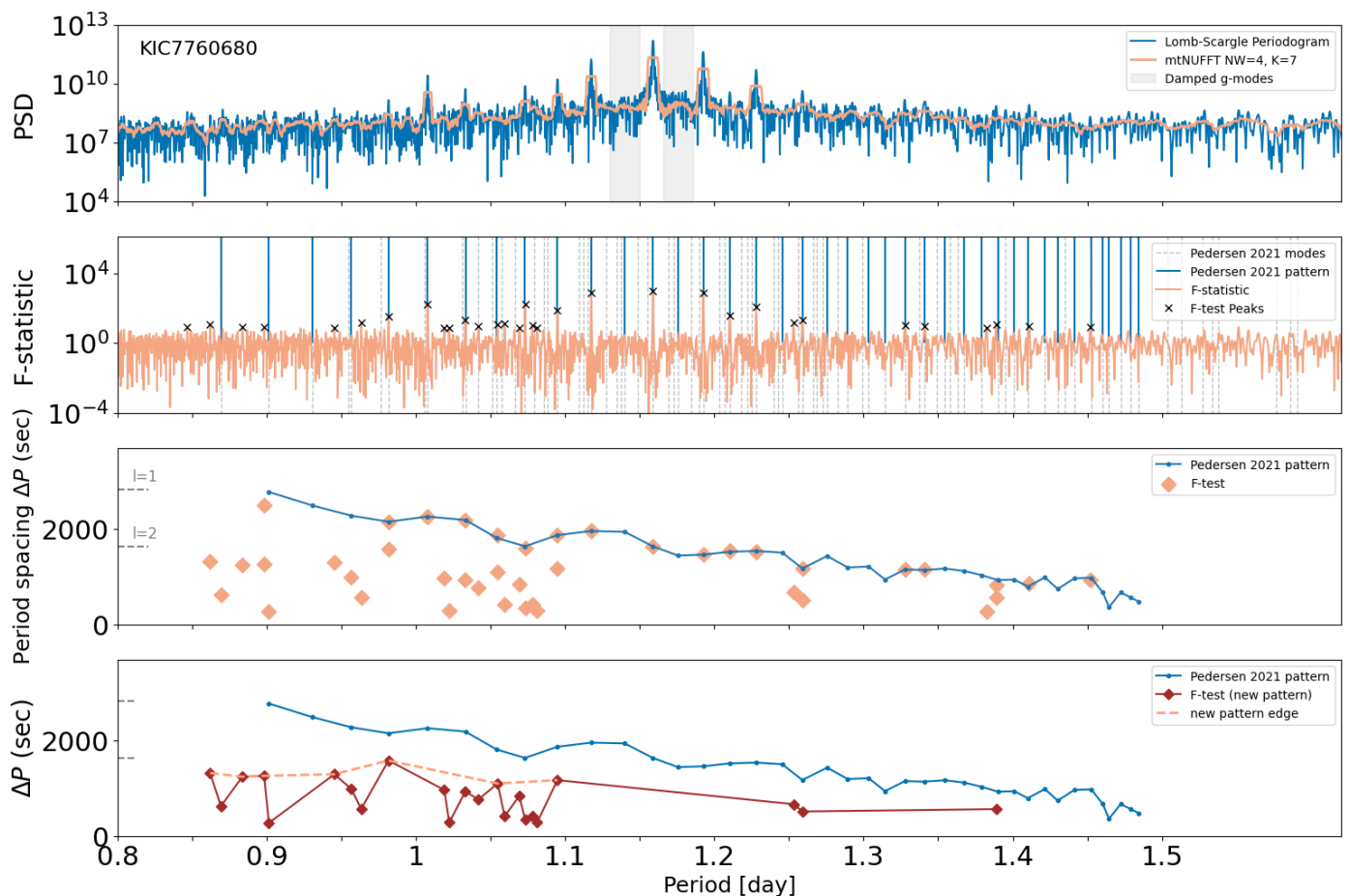


Fig. 9. Comparison of our F-test detections with the period-spacing pattern reported by PD21 for KIC7760680. The top panel shows the mtNUFFT spectrum (orange) and LS periodogram (blue), suggesting the presence of damped g modes (grey). The second panel displays the F-statistic (orange) with our detected modes (black crosses) and PD21 modes (grey dashed lines); modes belonging to the primary period-spacing pattern are highlighted in blue. In the third panel, orange diamonds mark our detections matching the PD21 primary pattern (blue curve) according to the match criteria in Table 1, while additional orange points denote secondary ΔP sequences from unmatched and nearby PD21 modes beyond the 3σ threshold. The bottom panel shows a secondary pattern (brown) near the expected position of $l = 2$ modes (grey dashed line on the y-axis), outlined by a dashed orange line.

reported by PD21. We also observe the presence of an additional period-spacing pattern, potentially corresponding to modes of degree $l = 2$. Additionally, we note that two missing frequencies adjacent to the main peak in the period-spacing pattern were not detected by the F-test, likely due to low power (unresolved modes) or damping broadening their frequency profiles.

KIC3240411, in contrast, represents a different case. It is the hottest known SPB with a dense and complex power spectrum of dipole modes (Szweczuk & Daszyńska-Daszkiewicz 2018). Despite four years of Kepler data, several extracted peaks remain difficult to interpret, with many identified as possible combination frequencies or unresolved signals. This makes KIC3240411 a demanding but valuable testbed to assess whether new approaches can outperform the standard iterative prewhitening procedure in disentangling independent g-mode frequencies. Similar to KIC7760680, we find secondary period spacing patterns as shown in Figure 10. After the secondary pattern is automatically constructed using modes lying below the PD21 pattern, we manually pick out features such as a potential dip in the pattern, which could tell us about processes such as mode trapping. (Szweczuk & Daszyńska-Daszkiewicz 2018) also point multiple possible patterns in this star that are similar to the ones we find.

Note that the g mode in KIC3240411 with a period of ≈ 1.1 d has a high amplitude but a weak F-statistic, which is why it is not detected by the F-test. This behaviour suggests the presence of resonant, damped, or modulated g modes, which we will discuss in detail in a forthcoming paper.

We provide the analogous figures to Figs. 9 and 10 for the 24 additional SPB stars treated in Pedersen et al. (2021) in Appendix A. The automatic identification of period-spacing patterns, as demonstrated for KIC7760680, differs for other stars depending on the specific mode distributions and morphological features present in their spectra. We apply an automatic approach to first find secondary patterns and manually check them to find general trends and peculiar features.

Overall, while we find less frequencies than in PD21, we present an efficient and more statistically sound approach to deduce mode frequencies and period spacing patterns. Asteroseismic modelling may likely still need prewhitening for sufficient g-mode detection and pattern recognition to secure spacing patterns. Yet, using our method, one could start off with a list of frequencies to help expedite this process and detect g modes with long lifetimes more securely than combined frequency and time domain analysis in an iterative manner.

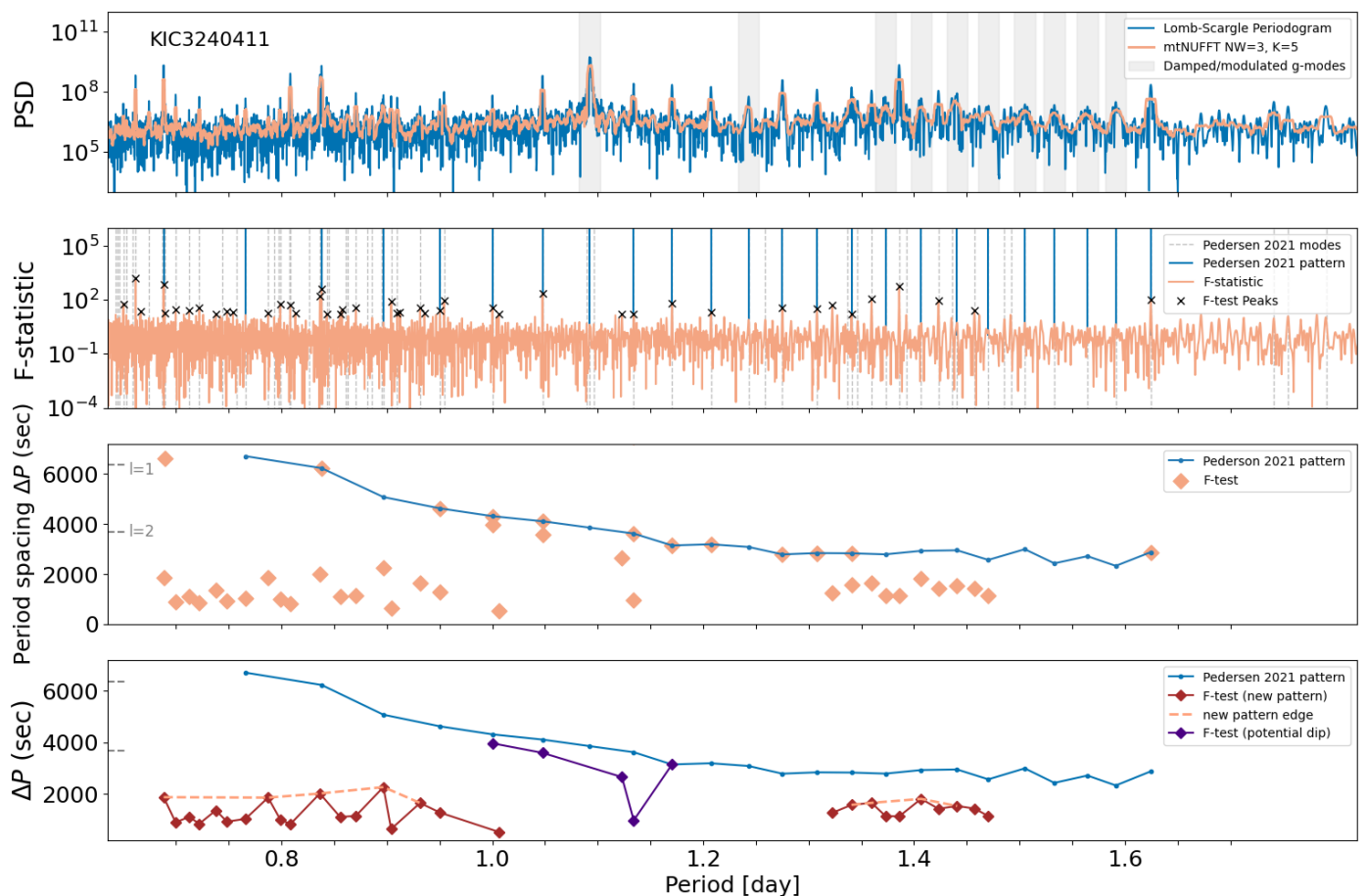


Fig. 10. Same as Fig. 9, but for KIC3240411, with the addition of a potential dip feature in the last panel (shown in violet). Here, the new period-spacing pattern (brown) is divided into separate segments.

5. Conclusions and outlook

The new frequency analysis methodology presented in this paper, which is based on the multitaper NUFFT periodogram and its extension with the F-test, is computationally efficient and offers the potential to help understand the content of the frequency spectra of SPB pulsators and the morphology of their period spacing patterns. Such observational information thereby aids in disentangling the excitation mechanisms and behaviour of g modes in SPB and other main-sequence pulsators, such as γ Doradus stars.

While we tuned our application to the challenging case of g mode detection, there is no mathematical reason why our method could not also be applied to other types of pulsators that require a prewhitening procedure before asteroseismology can be performed. Prewhitening involves repeated computation of the LS or similar types of computationally efficient periodograms. However, extraction of the highest-amplitude or highest-SNR signal, followed by sinusoidal fitting in the time domain from non-linear regression is cumbersome. It requires fitting the entire multi-sinusoidal model using a non-linear least-squares approach at each step. The computational cost scales roughly as $O(INN_f^3)$, where N is the number of time samples, N_f the number of extracted frequencies, and I the number of iterations per fit. This cubic scaling in N_f makes the method prohibitively expensive when hundreds of g-modes are present. By contrast, linear prewhitening (using LS with linear sinusoidal refinements) scales more gently as $O(N \log N + N_f M + N_f IN)$,

where M is the number of frequency bins. While more efficient than non-linear prewhitening, it grows linearly with N_f and remains costly for dense SPB spectra. Above all, use of any of such techniques implies data manipulation by subtracting imperfect regression models numerous times before the final list of significant frequencies is deduced. This ‘systematic error’ is propagated along the asteroseismic modelling process because the frequencies on this list are subsequently used as input to derive interpretable observables for asteroseismic interpretations, such as mode period spacing patterns.

The multitaper F-test is substantially faster because it evaluates significance for all frequencies simultaneously with complexity $O(KN \log N + MK)$, scaling only with the number of tapers K and remaining independent of N_f . This makes the F-test at least an order of magnitude faster than prewhitening approaches. While we find our approach to deliver less frequencies, it is complementary to prewhitening and does not suffer from iterative data manipulation. In this sense, our methodology brings new opportunities for future applications to g-mode pulsators, whose most important asteroseismic observables – the modes’ period spacing patterns – may suffer from imperfections of the time-consuming prewhitening procedure (Bowman & Michielsen 2021). Our method is entirely suitable to perform fast and objective frequency extraction, serving as an initial procedure to apply mode identification and asteroseismology to large populations of main-sequence pulsators as those in Balona et al. (2011); Mombarg et al. (2024). This would deliver a complementary approach to ‘boutique modelling’ of particular stars

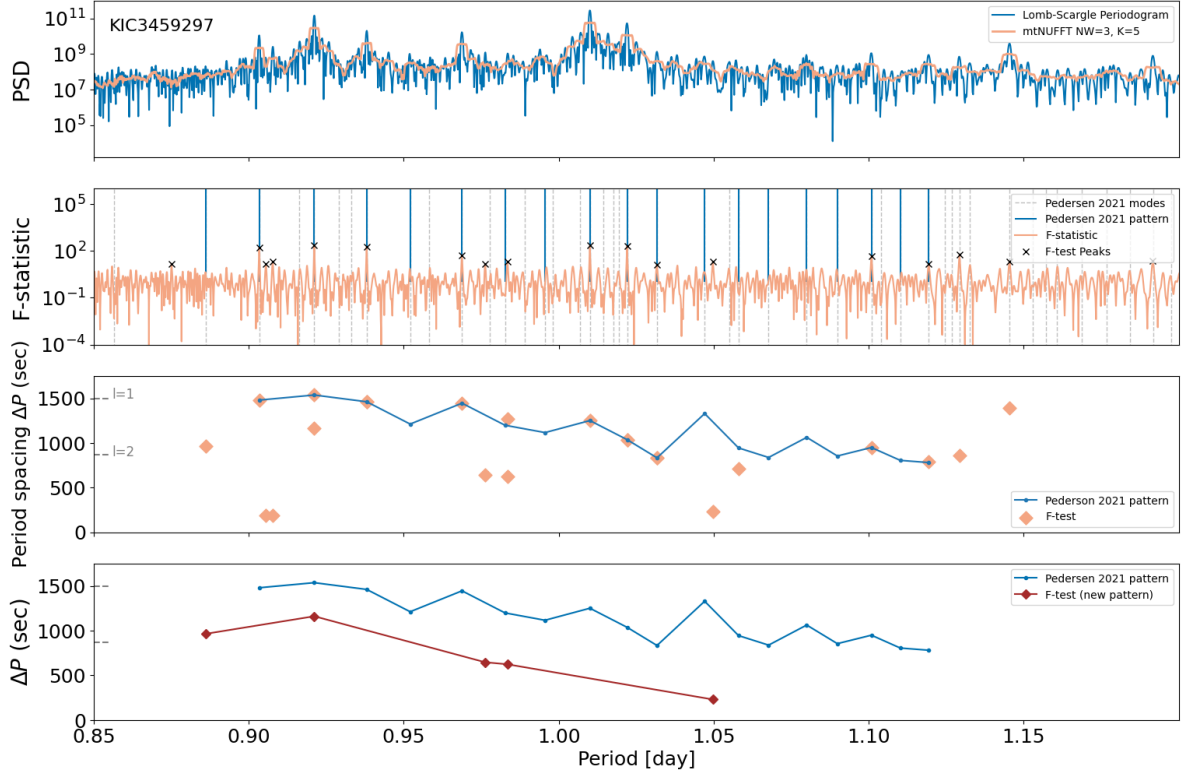
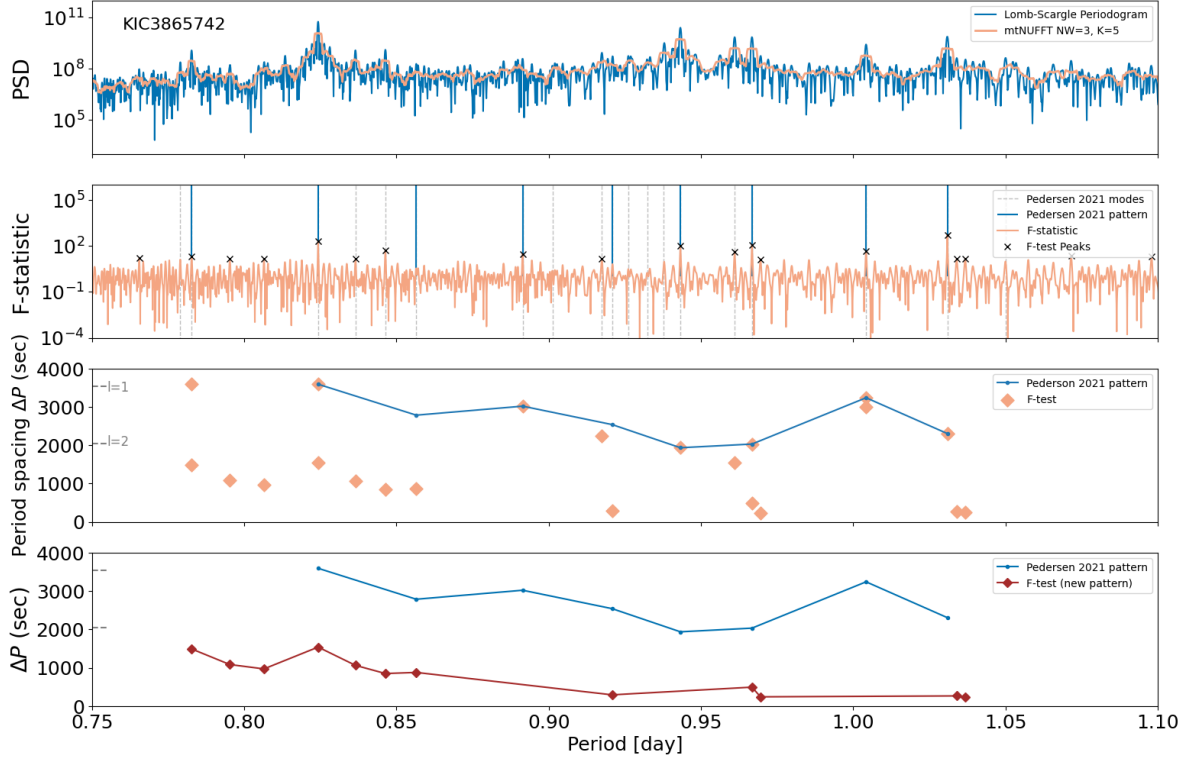
or small samples of pulsators as treated by Pedersen et al. (2021). Our fast frequency extraction and period search method can potentially pave the way to test and calibrate stellar structure and evolution models from large samples of intermediate- and high-mass pulsators.

The multitaper F-test also provides more information than the power spectrum alone. In addition to precisely identifying statistically significant oscillations in the Fourier domain, it also carries diagnostic value on the underlying physical excitation mechanism. For example, while a purely periodic g mode will typically yield both high power and a strong F-test detection, a mode with high amplitude but a weak F-statistic may instead suggest the presence of local or partial wave damping in the stellar interior or near the surface of the star. This opens up opportunities for the improvement of non-adiabatic asteroseismology, and we plan to dedicate a separate future study to the level of mode damping occurring in the SPB sample treated here.

Acknowledgements. AAP is supported by an LSST-DA Catalyst Fellowship; this publication was thus made possible through the support of Grant 62192 from the John Templeton Foundation to LSST-DA. CA receives funding from the European Research Council (ERC) under the Horizon Europe programme (Synergy Grant agreement N°101071505: 4D-STAR). JVB acknowledges funding from the European Research Council (Consolidator Grant N°101000296: DipolarSound). MGP recognizes support by the Professor Harry Messel Research Fellowship in Physics Endowment, at the University of Sydney. While partially funded by the European Union, views and opinions expressed are however those of the authors only and do not necessarily reflect those of the European Union or the European Research Council. Neither the European Union nor the granting authority can be held responsible for them.

References

- Aerts, C. 2021, *Reviews of Modern Physics*, 93, 015001
- Aerts, C., Augustson, K., Mathis, S., et al. 2021, *A&A*, 656, A121
- Aerts, C., Bowman, D. M., Simon-Díaz, S., et al. 2018a, *MNRAS*, 476, 1234
- Aerts, C., Christensen-Dalsgaard, J., & Kurtz, D. 2010, *Asteroseismology, Astronomy and Astrophysics Library* (Springer Netherlands)
- Aerts, C., Mathis, S., & Rogers, T. M. 2019, *ARA&A*, 57, 35
- Aerts, C., Molenberghs, G., & De Ridder, J. 2023, *A&A*, 672, A183
- Aerts, C., Molenberghs, G., Michielsen, M., et al. 2018b, *ApJS*, 237, 15
- Aerts, C. & Rogers, T. M. 2015, *ApJ*, 806, L33
- Aerts, C., Van Reeth, T., Mombarg, J. S. G., & Hey, D. 2025, *A&A*, 695, A214
- Anders, E. H., Lecoanet, D., Cantiello, M., et al. 2023, *Nature Astronomy*, 7, 1228
- Antoci, V., Cunha, M. S., Bowman, D. M., et al. 2019, *MNRAS*, 490, 4040
- Balona, L. A., Pigulski, A., De Cat, P., et al. 2011, *MNRAS*, 413, 2403
- Blomme, R., Mahy, L., Catala, C., et al. 2011, *A&A*, 533, A4
- Bouabid, M. P., Dupret, M. A., Salmon, S., et al. 2013, *MNRAS*, 429, 2500
- Bowman, D. M., Burssens, S., Pedersen, M. G., et al. 2019, *Nature Astronomy*, 3, 760
- Bowman, D. M., Burssens, S., Simón-Díaz, S., et al. 2020, *A&A*, 640, A36
- Bowman, D. M. & Michielsen, M. 2021, *A&A*, 656, A158
- Bowman, D. M., Van Daele, P., Michielsen, M., & Van Reeth, T. 2024, *A&A*, 692, A49
- Breger, M., Stich, J., Garrido, R., et al. 1993, *A&A*, 271, 482
- Burssens, S., Simón-Díaz, S., Bowman, D. M., et al. 2020, *A&A*, 639, A81
- Cantiello, M. & Braithwaite, J. 2019, *ApJ*, 883, 106
- Cantiello, M., Langer, N., Brott, I., et al. 2009, *A&A*, 499, 279
- Christophe, S., Ballot, J., Ouazzani, R. M., Antoci, V., & Salmon, S. J. A. J. 2018, *A&A*, 618, A47
- Degroote, P., Aerts, C., Baglin, A., et al. 2010a, *Nature*, 464, 259
- Degroote, P., Aerts, C., Baglin, A., et al. 2010b, *Nature*, 464, 259
- Edelmann, P. V. F., Ratnasingam, R. P., Pedersen, M. G., et al. 2019, *ApJ*, 876, 4
- Elliott, A., Richardson, N. D., Pablo, H., et al. 2022, *MNRAS*, 509, 4246
- Gaia Collaboration, De Ridder, J., Ripepi, V., Aerts, C., & Palaversa, L. 2023, *A&A*, 674, A36
- García, R. A. & Ballot, J. 2019, *Living Reviews in Solar Physics*, 16, 4
- Gilliland, R. L., Brown, T. M., Christensen-Dalsgaard, J., et al. 2010, *PASP*, 122, 131
- Hekker, S. & Christensen-Dalsgaard, J. 2017, *A&A Rev.*, 25, 1
- Hey, D. & Aerts, C. 2024, *A&A*, 688, A93
- Horst, L., Edelmann, P. V. F., Andrásy, R., et al. 2020, *A&A*, 641, A18
- Kourniotis, M., Cidale, L. S., Kraus, M., Ruiz Diaz, M. A., & Alberici Adam, A. 2025, *A&A*, 697, A152
- Krtićka, J. & Feldmeier, A. 2018, *A&A*, 617, A121
- Krtićka, J. & Feldmeier, A. 2021, *A&A*, 648, A79
- Lecoanet, D., Bowman, D. M., & Van Reeth, T. 2022, *MNRAS*, 512, L16
- Lecoanet, D., Cantiello, M., Quataert, E., et al. 2019, *ApJ*, 886, L15
- Lehmann, H., Tkachenko, A., Semaan, T., et al. 2011, *A&A*, 526, A124
- Li, G., Van Reeth, T., Bedding, T. R., et al. 2020, *MNRAS*, 491, 3586
- Michielsen, M., Aerts, C., & Bowman, D. M. 2021, *A&A*, 650, A175
- Michielsen, M., Pedersen, M. G., Augustson, K. C., Mathis, S., & Aerts, C. 2019, *A&A*, 628, A76
- Miglio, A., Montalbán, J., Noels, A., & Eggenberger, P. 2008, *MNRAS*, 386, 1487
- Mombarg, J. S. G., Aerts, C., Van Reeth, T., & Hey, D. 2024, *A&A*, 691, A131
- Moravveji, E., Aerts, C., Pápics, P. I., Triana, S. A., & Vandoren, B. 2015, *A&A*, 580, A27
- Moravveji, E., Townsend, R. H. D., Aerts, C., & Mathis, S. 2016, *ApJ*, 823, 130
- Neiner, C., Floquet, M., Samadi, R., et al. 2012, *A&A*, 546, A47
- Neiner, C., Gutiérrez-Soto, J., Baudin, F., et al. 2009, *A&A*, 506, 143
- Neiner, C., Lee, U., Mathis, S., et al. 2020, *A&A*, 644, A9
- Pamyatnykh, A. A. 1999, *Acta Astron.*, 49, 119
- Pápics, P. I., Moravveji, E., Aerts, C., et al. 2014, *A&A*, 570, A8
- Pápics, P. I., Tkachenko, A., Aerts, C., et al. 2013, *A&A*, 553, A127
- Pápics, P. I., Tkachenko, A., Aerts, C., et al. 2015, *ApJ*, 803, L25
- Pápics, P. I., Tkachenko, A., Van Reeth, T., et al. 2017, *A&A*, 598, A74
- Patil, A. A., Eadie, G. M., Speagle, J. S., & Thomson, D. J. 2024, *AJ*, 168, 193
- Patil, A. A., Eadie, G. M., Speagle, J. S., & Thomson, D. J. 2025, *AJ*, 170, 7
- Pedersen, M. G. 2020, PhD thesis, KU Leuven, Belgium
- Pedersen, M. G. 2022, *ApJ*, 930, 94
- Pedersen, M. G., Aerts, C., Pápics, P. I., et al. 2021, *Nature Astronomy*, 5, 715
- Pedersen, M. G., Aerts, C., Pápics, P. I., & Rogers, T. M. 2018, *A&A*, 614, A128
- Pedersen, M. G. & Bildsten, L. 2025, *MNRAS*, 539, 2742
- Pedersen, M. G., Chowdhury, S., Johnston, C., et al. 2019, *ApJ*, 872, L9
- Ramaramantsoa, T., Ratnasingam, R., Shenar, T., et al. 2018, *MNRAS*, 480, 972
- Ratnasingam, R. P., Edelmann, P. V. F., & Rogers, T. M. 2020, *MNRAS*, 497, 4231
- Ratnasingam, R. P., Rogers, T. M., Chowdhury, S., et al. 2023, *A&A*, 674, A134
- Rehm, R., Mombarg, J. S. G., Aerts, C., et al. 2024, *A&A*, 687, A175
- Rife, D. C. & Boorstyn, R. R. 1976, *The Bell System Technical Journal*, 55, 1389
- Schultz, W. C., Bildsten, L., & Jiang, Y.-F. 2022, *ApJ*, 924, L11
- Serebriakova, N., Tkachenko, A., & Aerts, C. 2024, *A&A*, 692, A245
- Sharma, A. N., Bedding, T. R., Saio, H., & White, T. R. 2022, *MNRAS*, 515, 828
- Shen, D.-X., Zhu, C.-H., Lü, G.-L., Lu, X.-z., & He, X.-l. 2024, *ApJS*, 275, 2
- Simón-Díaz, S., Godart, M., Castro, N., et al. 2017, *A&A*, 597, A22
- Slepian, D. 1978, *AT T Technical Journal*, 57, 1371
- Springford, A., Eadie, G. M., & Thomson, D. J. 2020, *AJ*, 159, 205
- Szewczuk, W. & Daszyńska-Daszkiewicz, J. 2017, *MNRAS*, 469, 13
- Szewczuk, W. & Daszyńska-Daszkiewicz, J. 2018, *MNRAS*, 478, 2243
- Szewczuk, W., Walczak, P., & Daszyńska-Daszkiewicz, J. 2021, *MNRAS*, 503, 5894
- Szewczuk, W., Walczak, P., Daszyńska-Daszkiewicz, J., & Moździerski, D. 2022, *MNRAS*, 511, 1529
- Thomson, D. J. 1982, *IEEE Proceedings*, 70, 1055
- Thomson, D. J. 2007, *IEEE Signal Processing Magazine*, 24, 20
- Tkachenko, A., Degroote, P., Aerts, C., et al. 2014, *MNRAS*, 438, 3093
- Townsend, R. H. D. 2005a, *MNRAS*, 360, 465
- Townsend, R. H. D. 2005b, *MNRAS*, 364, 573
- Townsend, R. H. D., Goldstein, J., & Zweibel, E. G. 2018, *MNRAS*, 475, 879
- Van Beeck, J., Bowman, D. M., Pedersen, M. G., et al. 2021, *A&A*, 655, A59
- Van Beeck, J., Van Hoolst, T., Aerts, C., & Fuller, J. 2024, *A&A*, 687, A265
- Van Reeth, T., Tkachenko, A., & Aerts, C. 2016, *A&A*, 593, A120
- Van Reeth, T., Tkachenko, A., Aerts, C., et al. 2015a, *A&A*, 574, A17
- Van Reeth, T., Tkachenko, A., Aerts, C., et al. 2015b, *ApJS*, 218, 27
- Vanon, R., Edelmann, P. V. F., Ratnasingam, R. P., Varghese, A., & Rogers, T. M. 2023, *ApJ*, 954, 171
- Zhang, C., Liu, C., Wu, Y., et al. 2018, *ApJ*, 854, 168
- Zhang, Z., Ren, Y., Jiang, B., Soszyński, I., & Jayasinghe, T. 2024, *ApJ*, 969, 81

Appendix A: Additional plots comparing the F-test detections and period spacing patterns from our work with those in Pedersen et al. (2021)

Fig. A.1. Comparison of our F-test detections with the period spacing patterns in PD21 for KIC3459297.

Fig. A.2. Comparison of our F-test detections with the period spacing patterns in PD21 for KIC3865742.

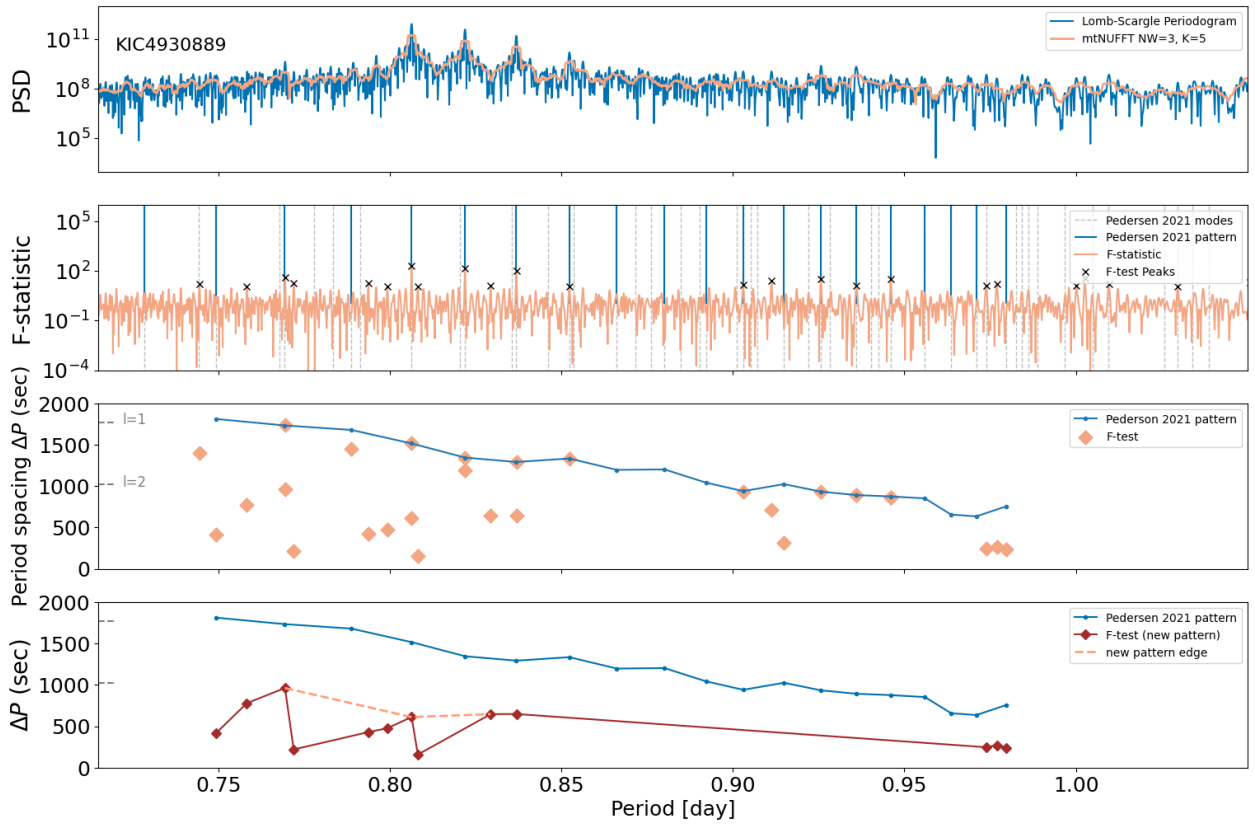


Fig. A.3. Comparison of our F-test detections with the period spacing patterns in PD21 for KIC4930889.

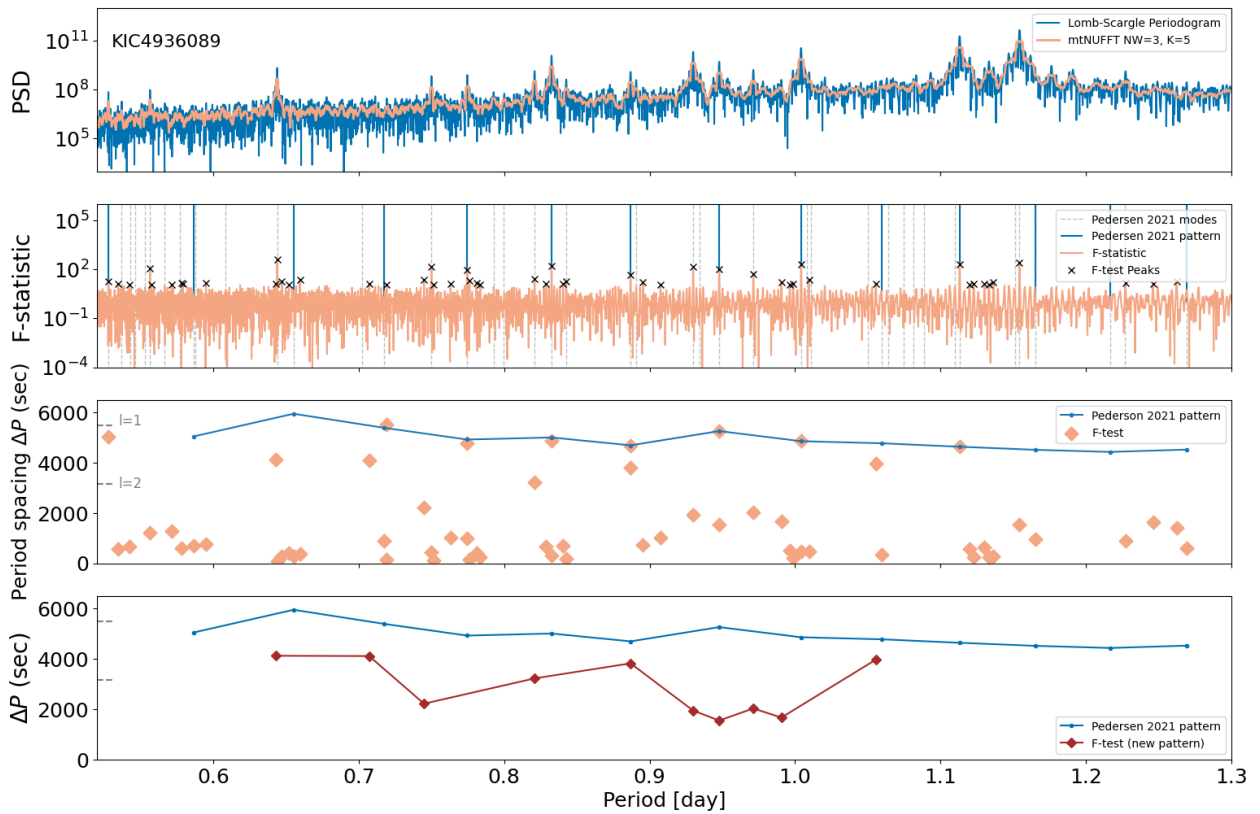


Fig. A.4. Comparison of our F-test detections with the period spacing patterns in PD21 for KIC4936089.

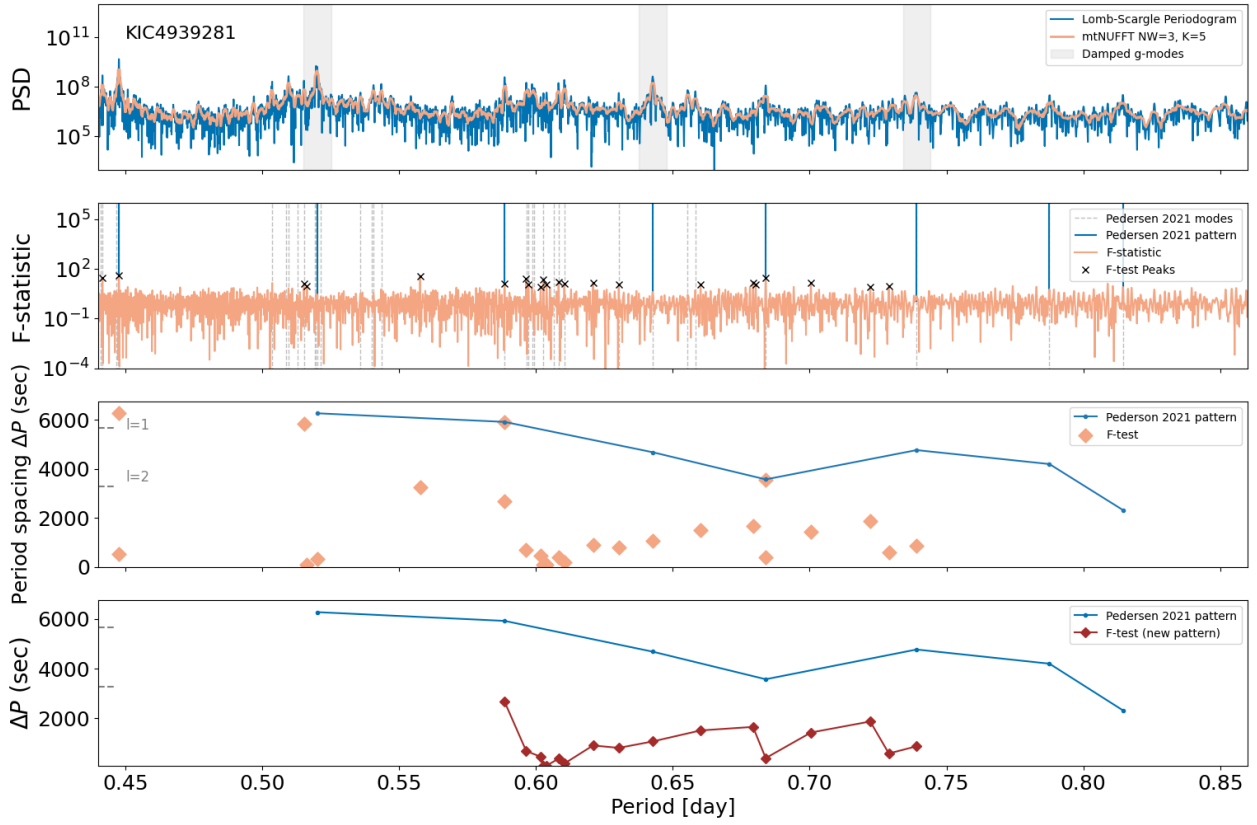


Fig. A.5. Comparison of our F-test detections with the period spacing patterns in PD21 for KIC4939281.

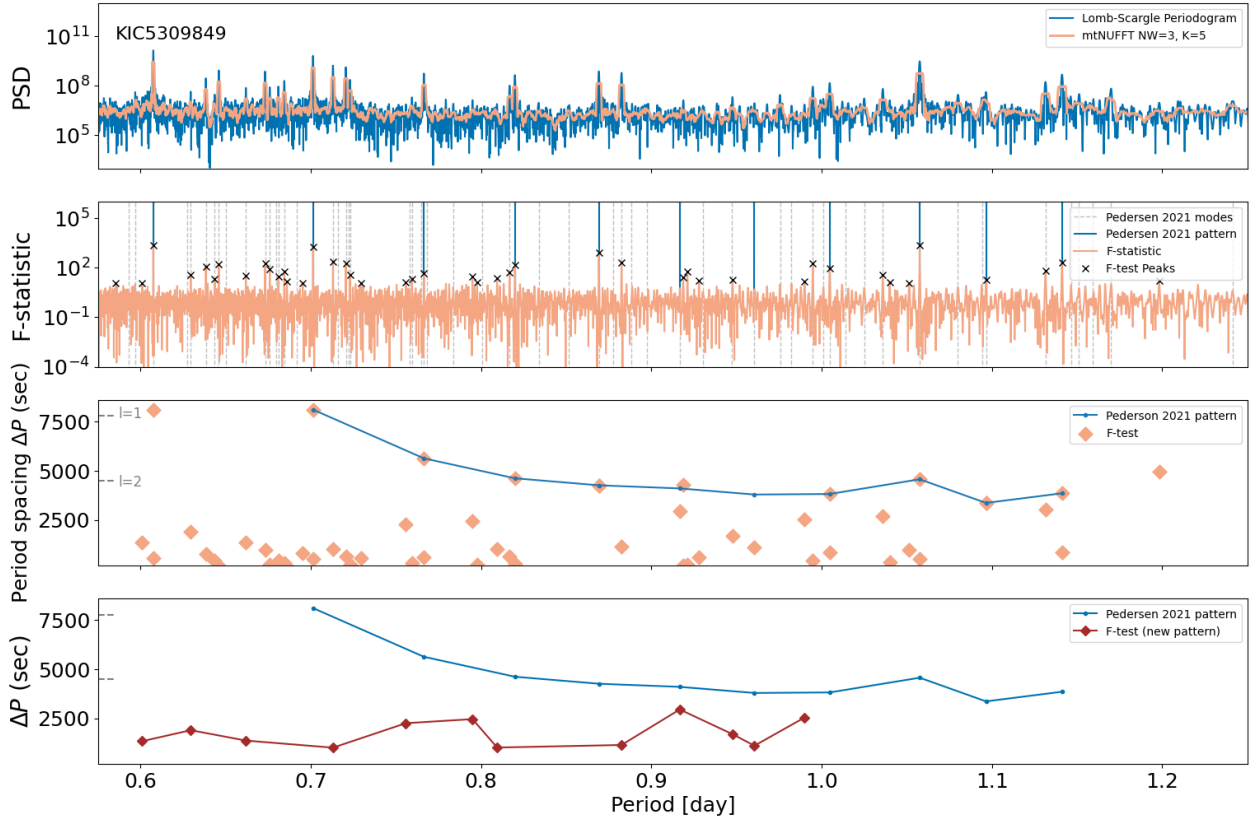


Fig. A.6. Comparison of our F-test detections with the period spacing patterns in PD21 for KIC5309849.

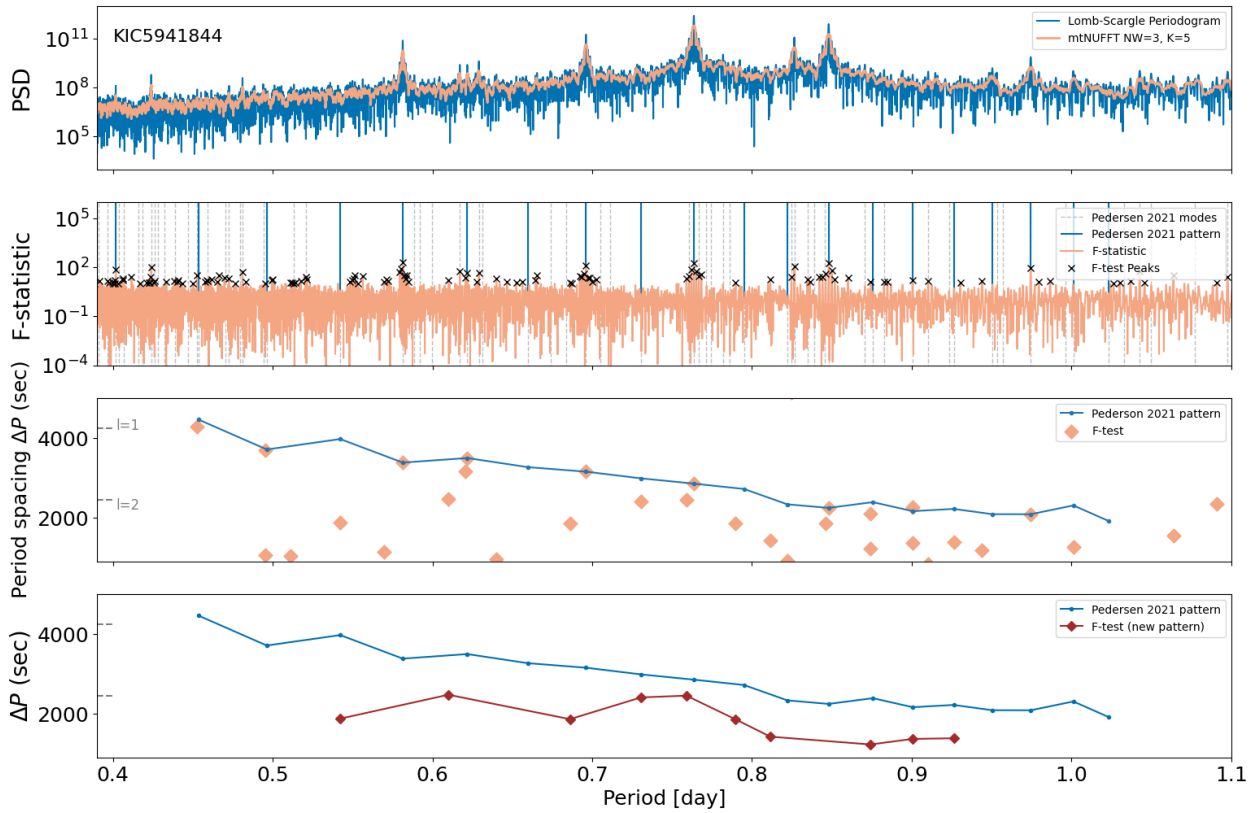


Fig. A.7. Comparison of our F-test detections with the period spacing patterns in PD21 for KIC5941844.

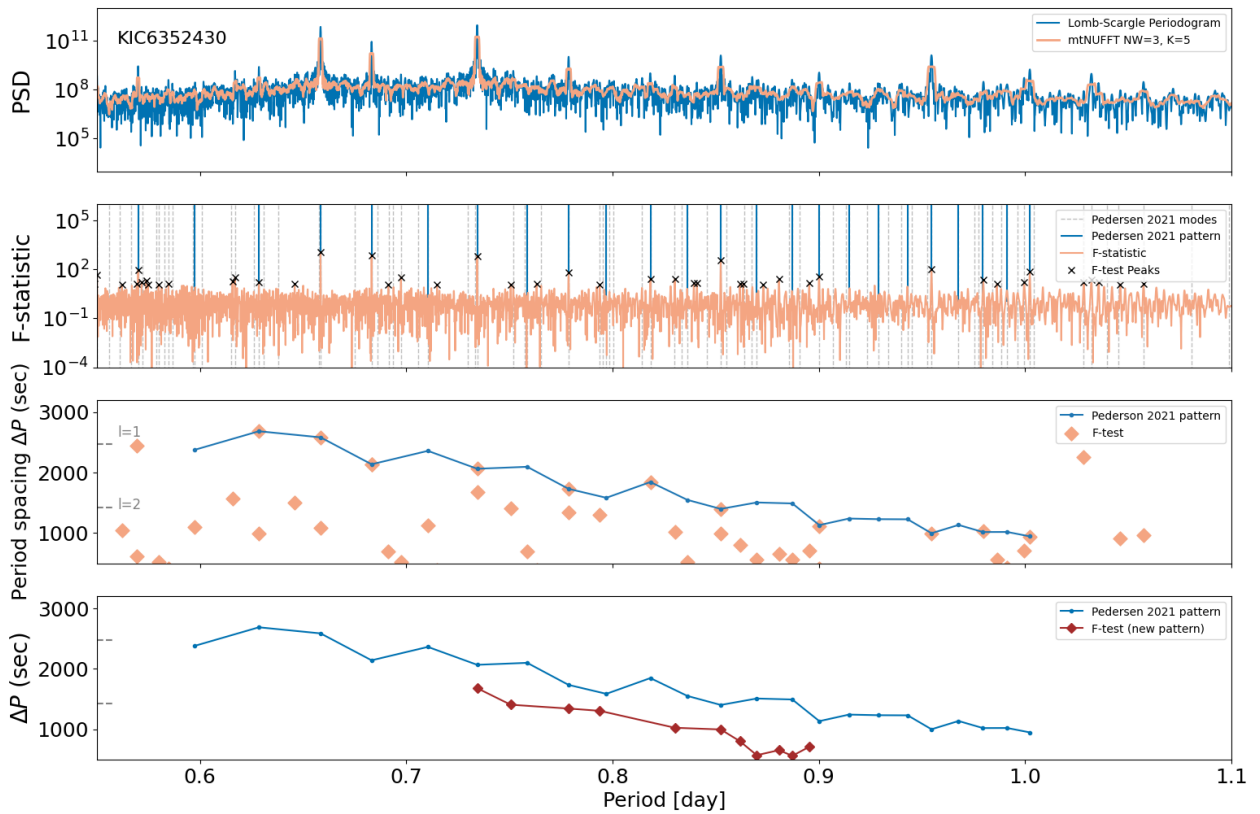


Fig. A.8. Comparison of our F-test detections with the period spacing patterns in PD21 for KIC6352430.

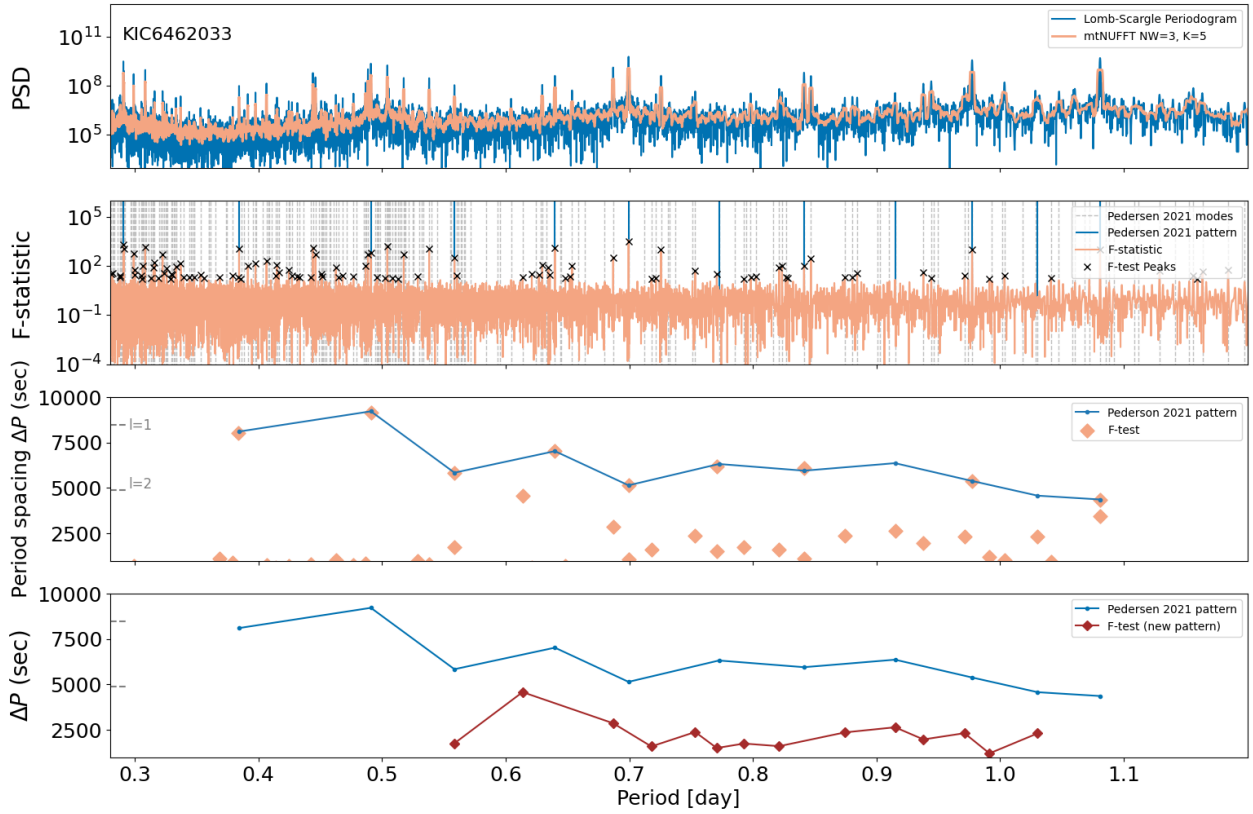


Fig. A.9. Comparison of our F-test detections with the period spacing patterns in PD21 for KIC6462033.

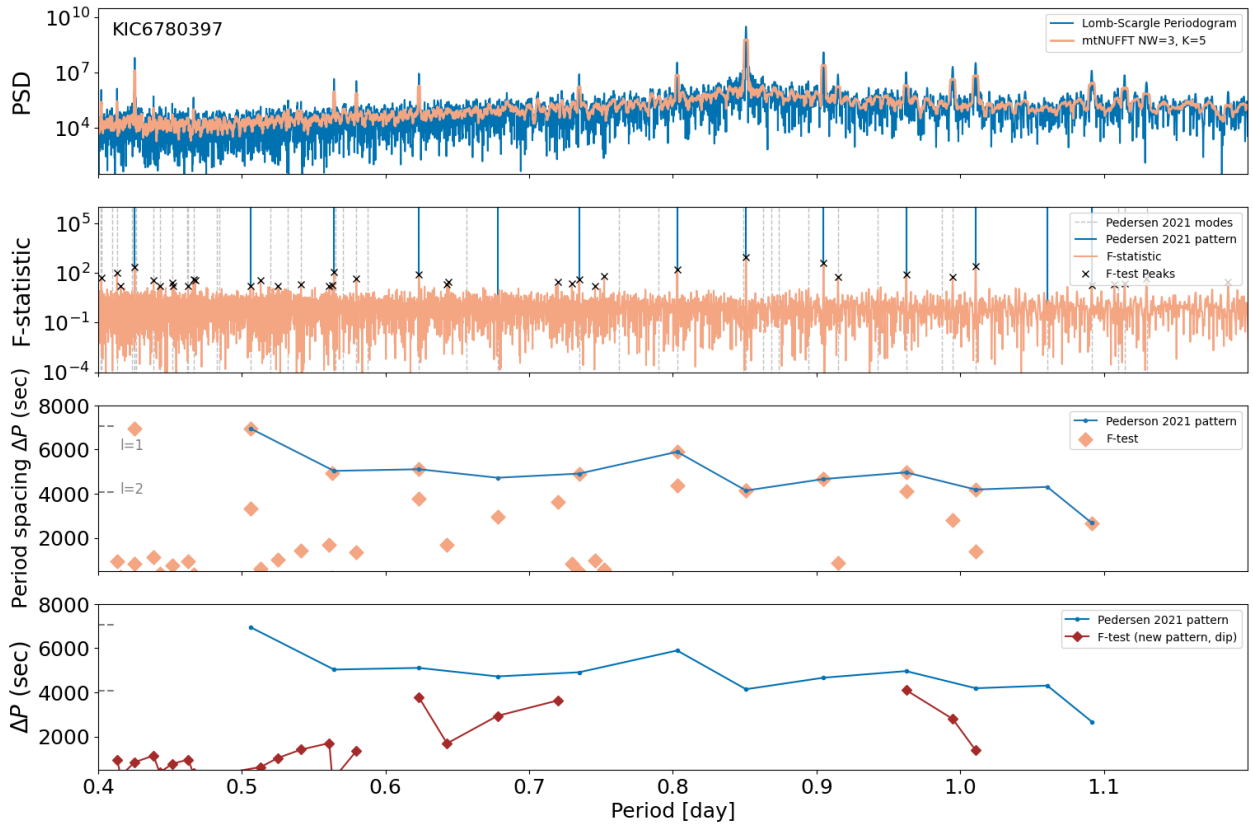


Fig. A.10. Comparison of our F-test detections with the period spacing patterns in PD21 for KIC6780397.

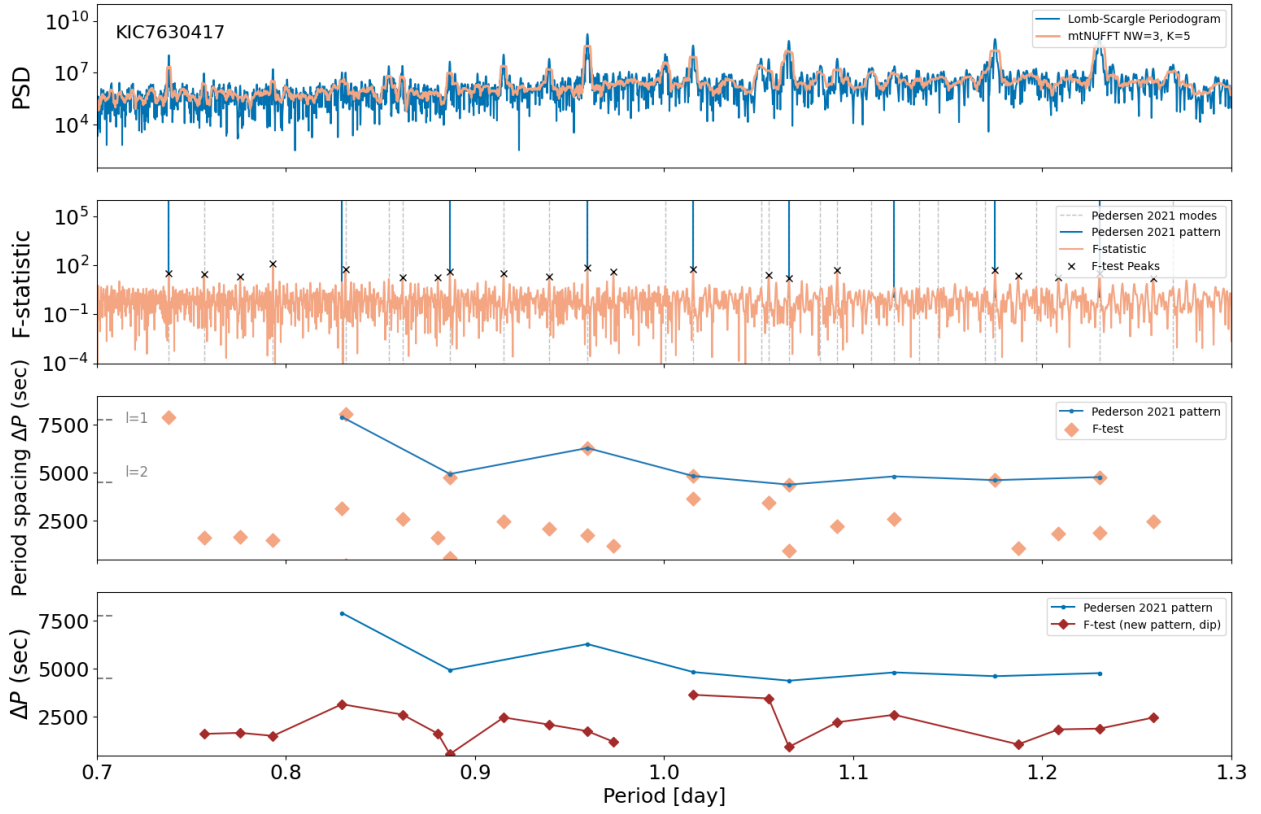


Fig. A.11. Comparison of our F-test detections with the period spacing patterns in PD21 for KIC7630417.

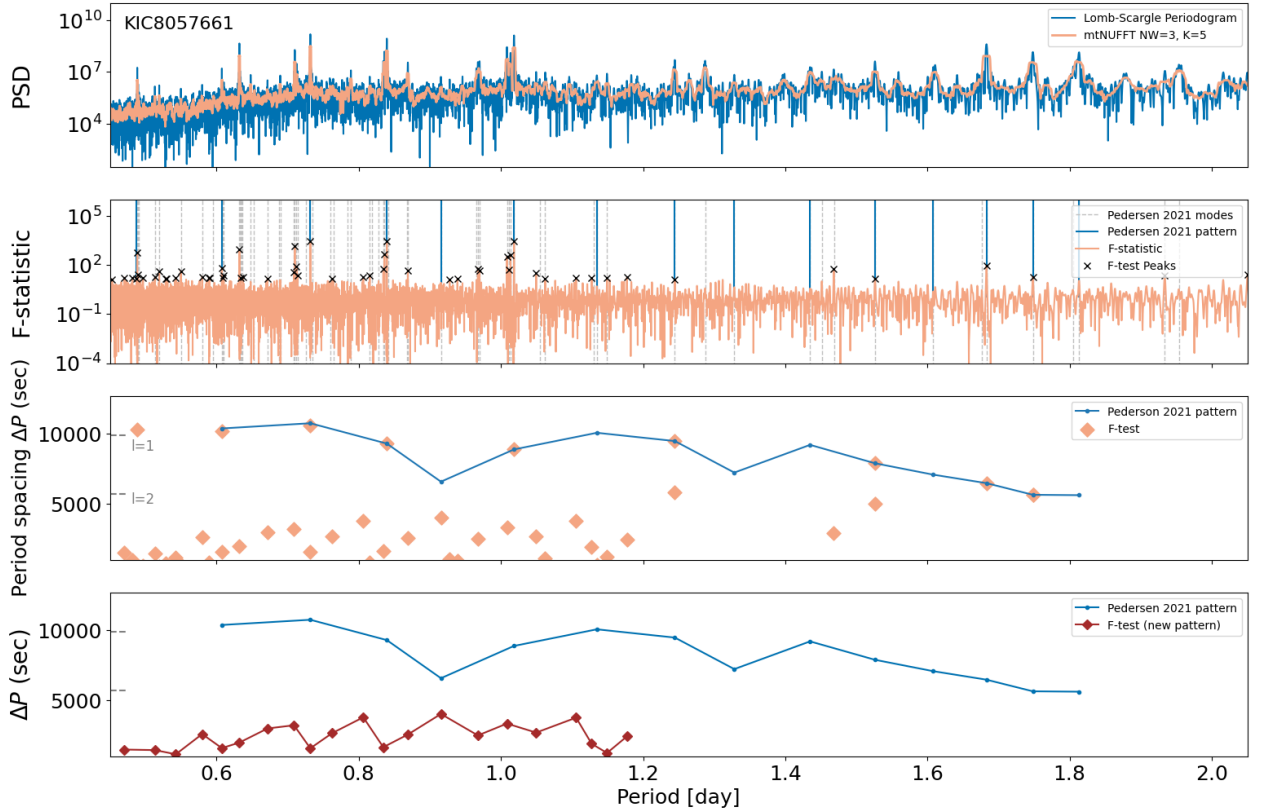


Fig. A.12. Comparison of our F-test detections with the period spacing patterns in PD21 for KIC8057661.

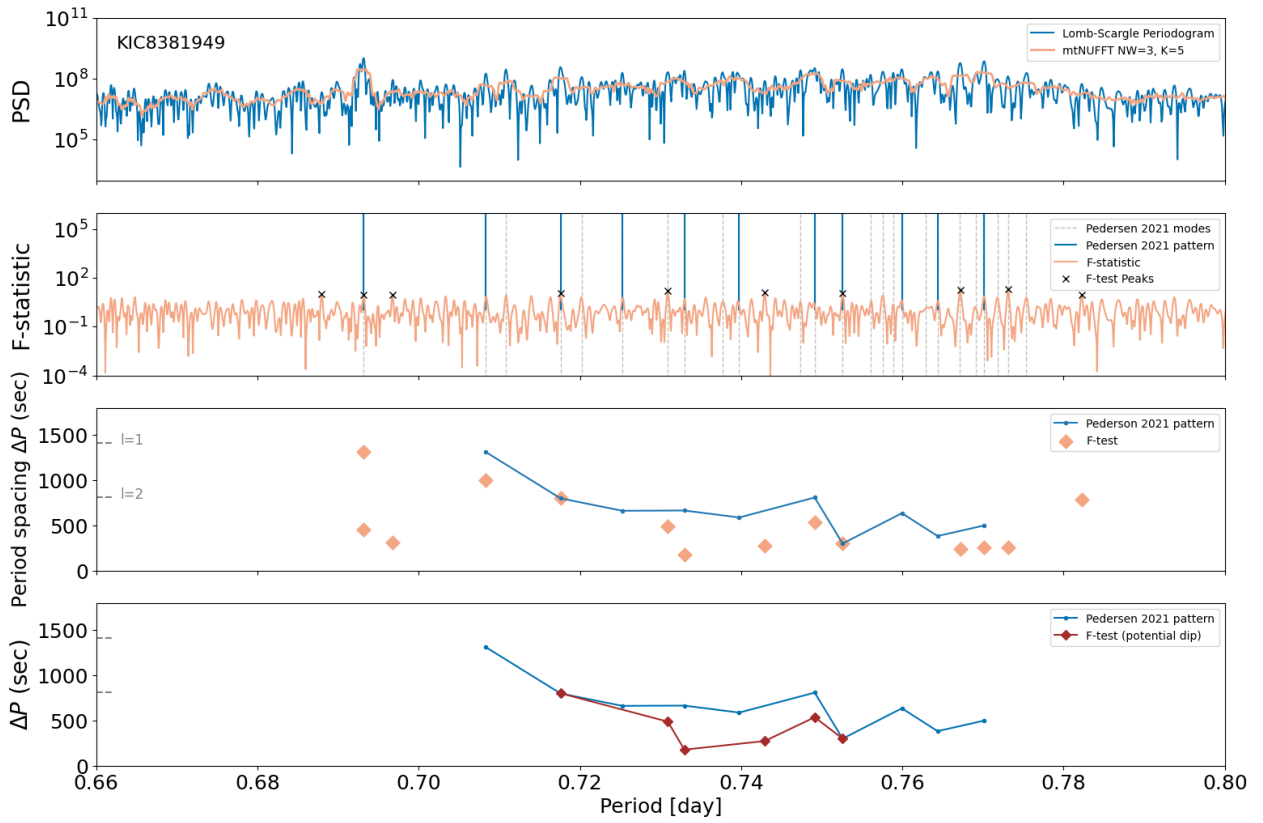


Fig. A.13. Comparison of our F-test detections with the period spacing patterns in PD21 for KIC8381949.

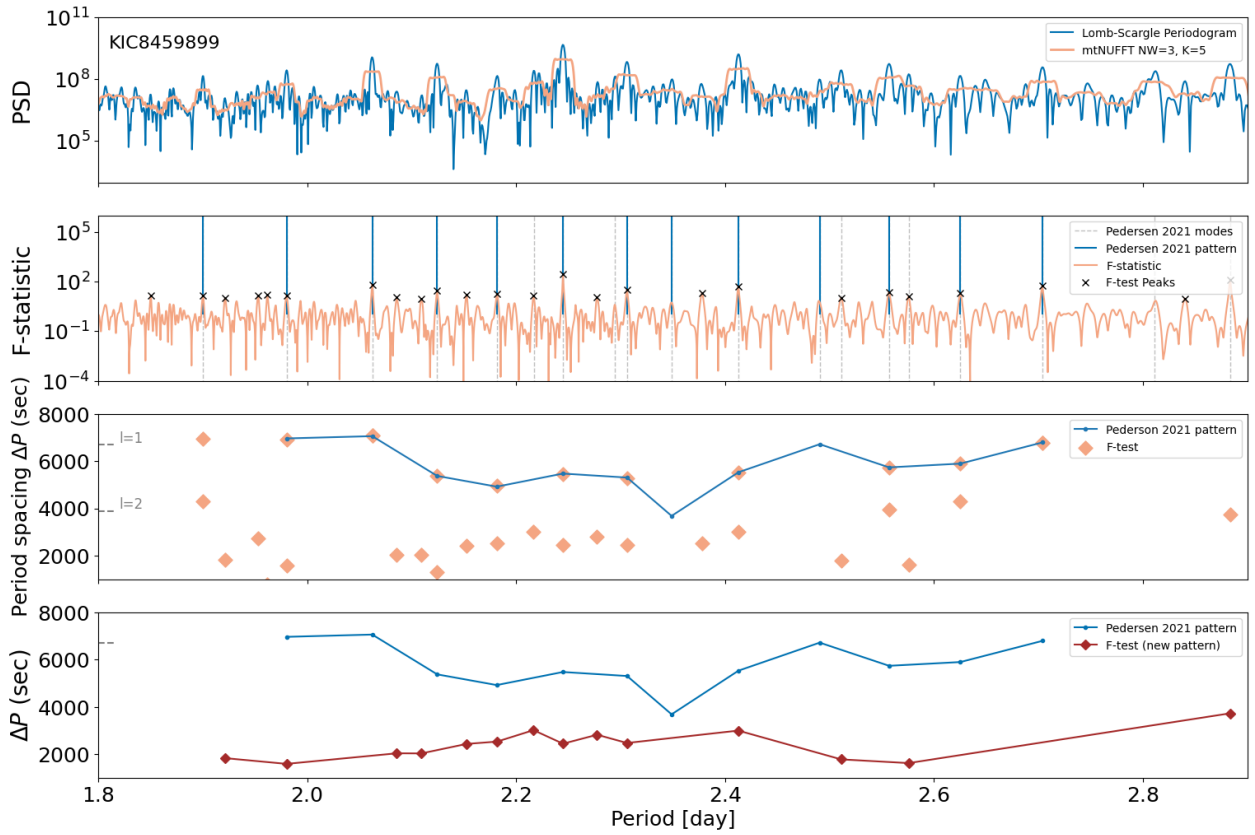


Fig. A.14. Comparison of our F-test detections with the period spacing patterns in PD21 for KIC8459899.

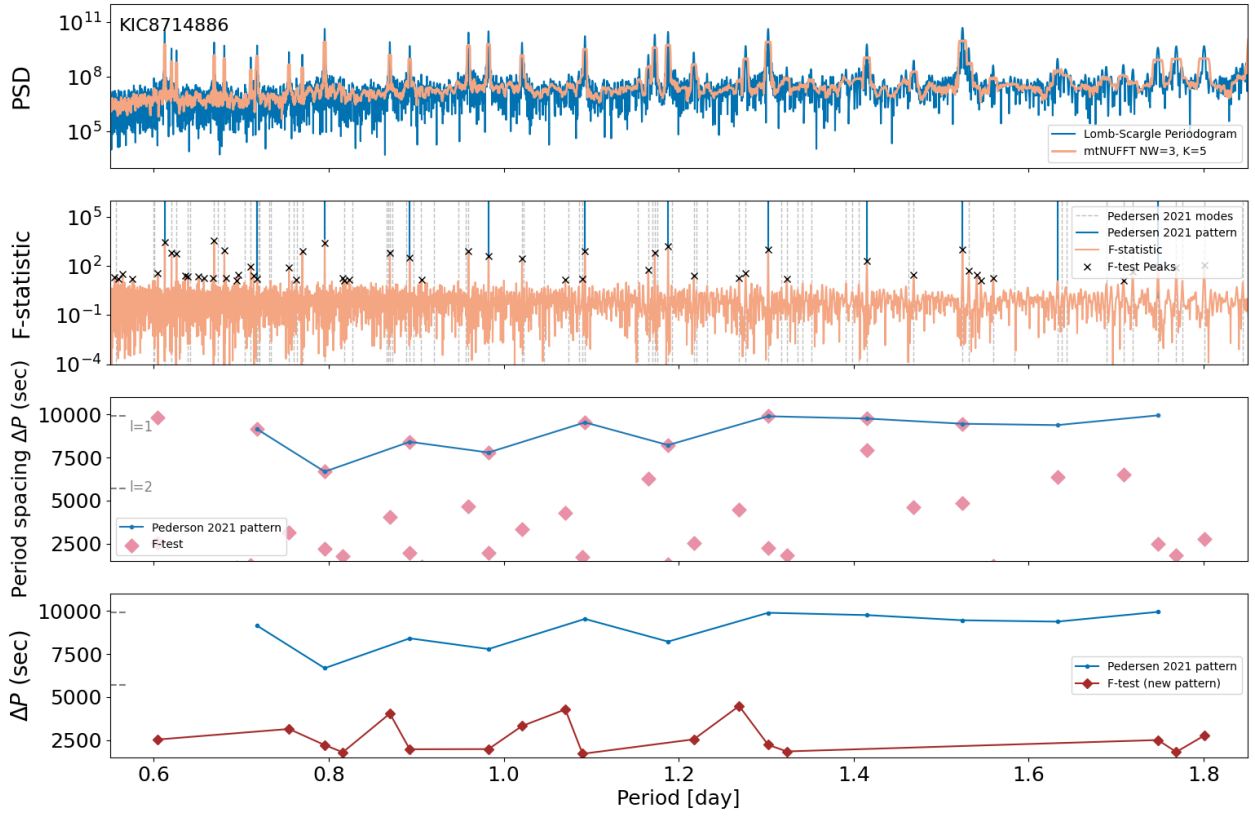


Fig. A.15. Comparison of our F-test detections with the period spacing patterns in PD21 for KIC8714886.

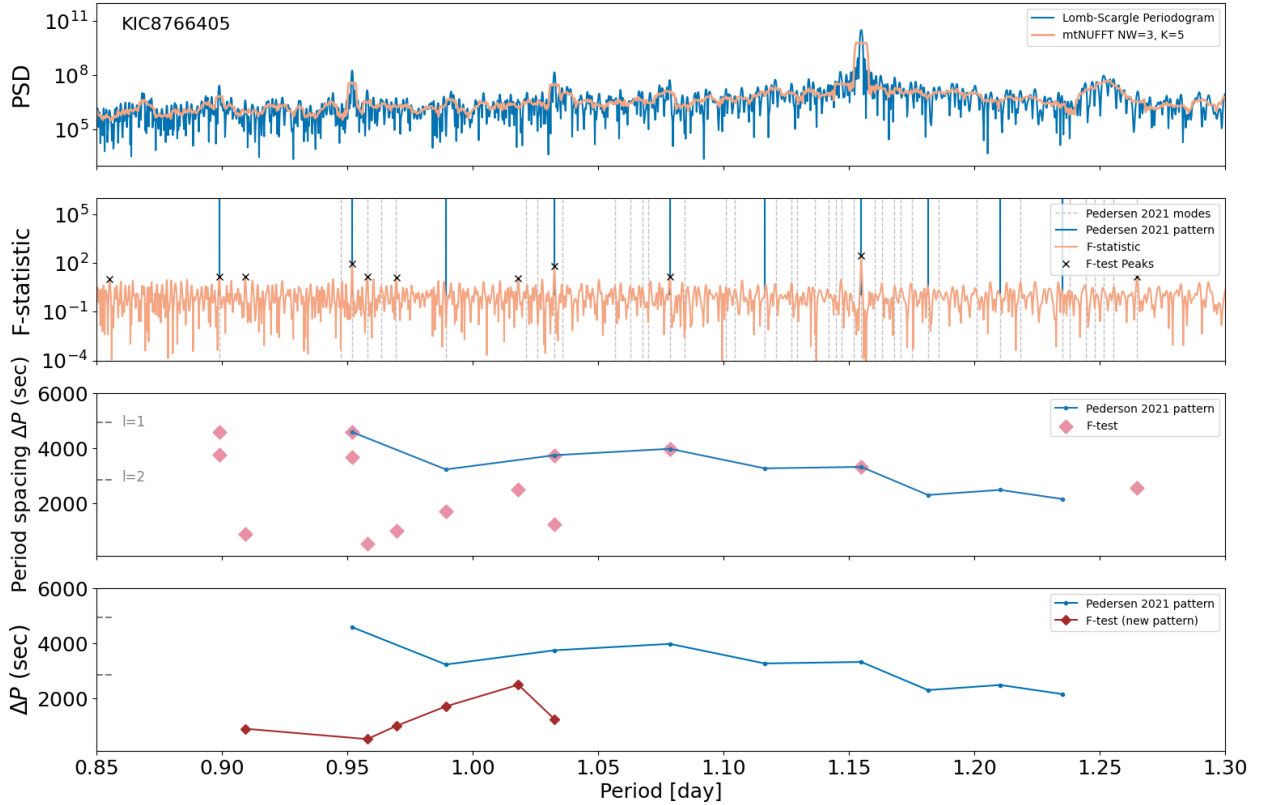


Fig. A.16. Comparison of our F-test detections with the period spacing patterns in PD21 for KIC8766405.

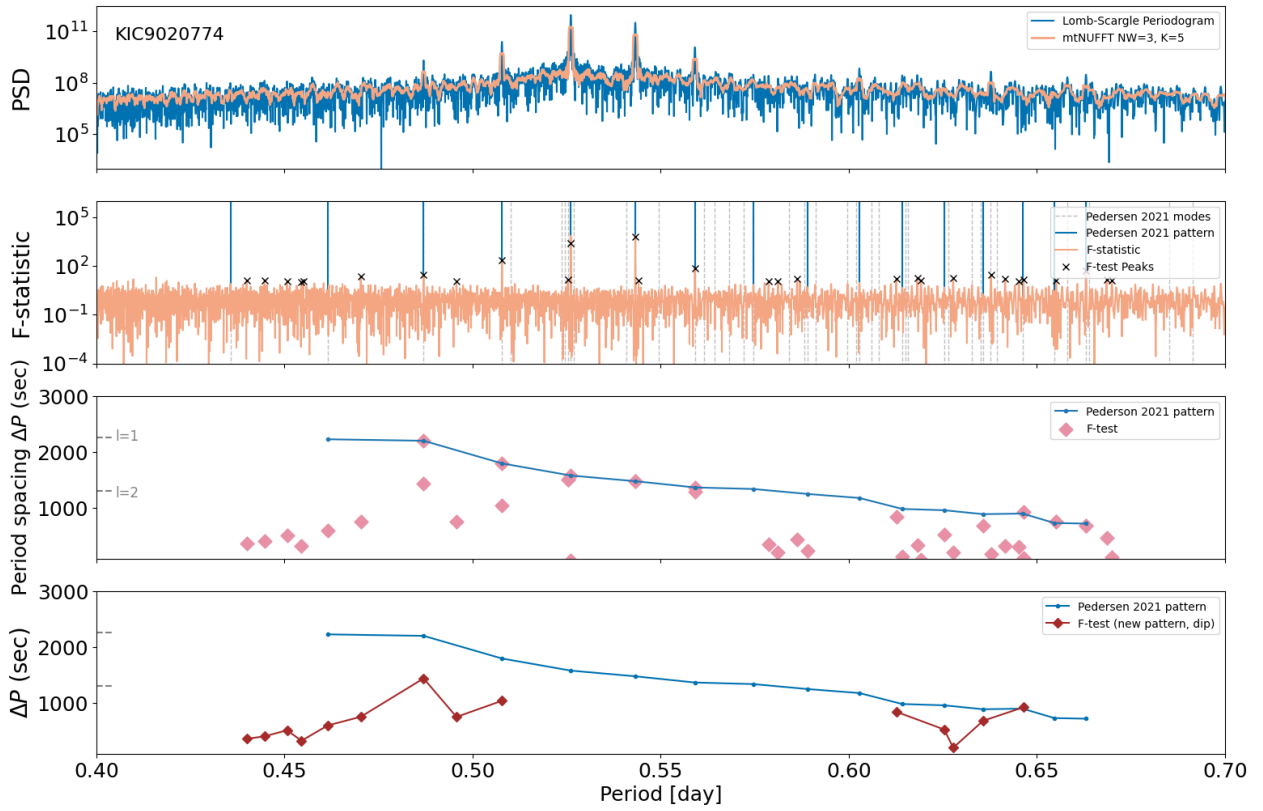


Fig. A.17. Comparison of our F-test detections with the period spacing patterns in PD21 for KIC9020774.

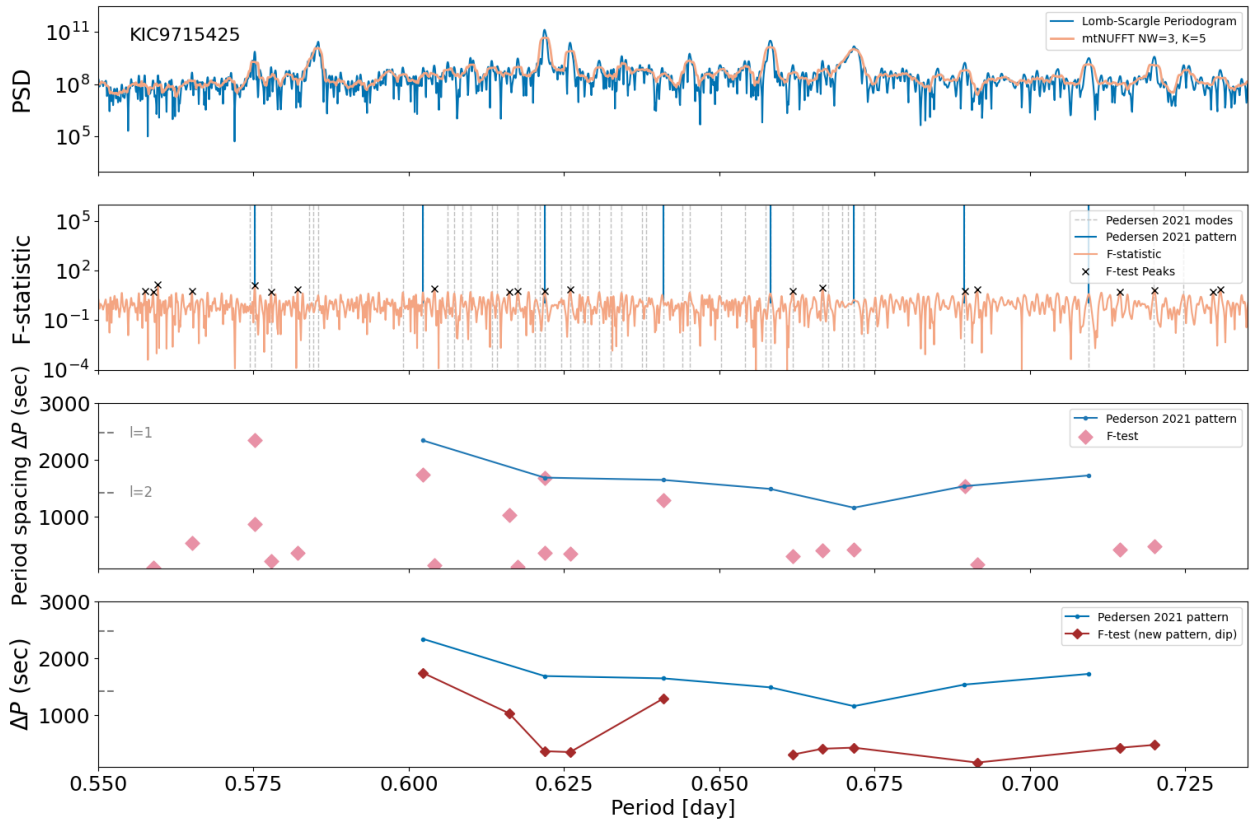


Fig. A.18. Comparison of our F-test detections with the period spacing patterns in PD21 for KIC9715425.

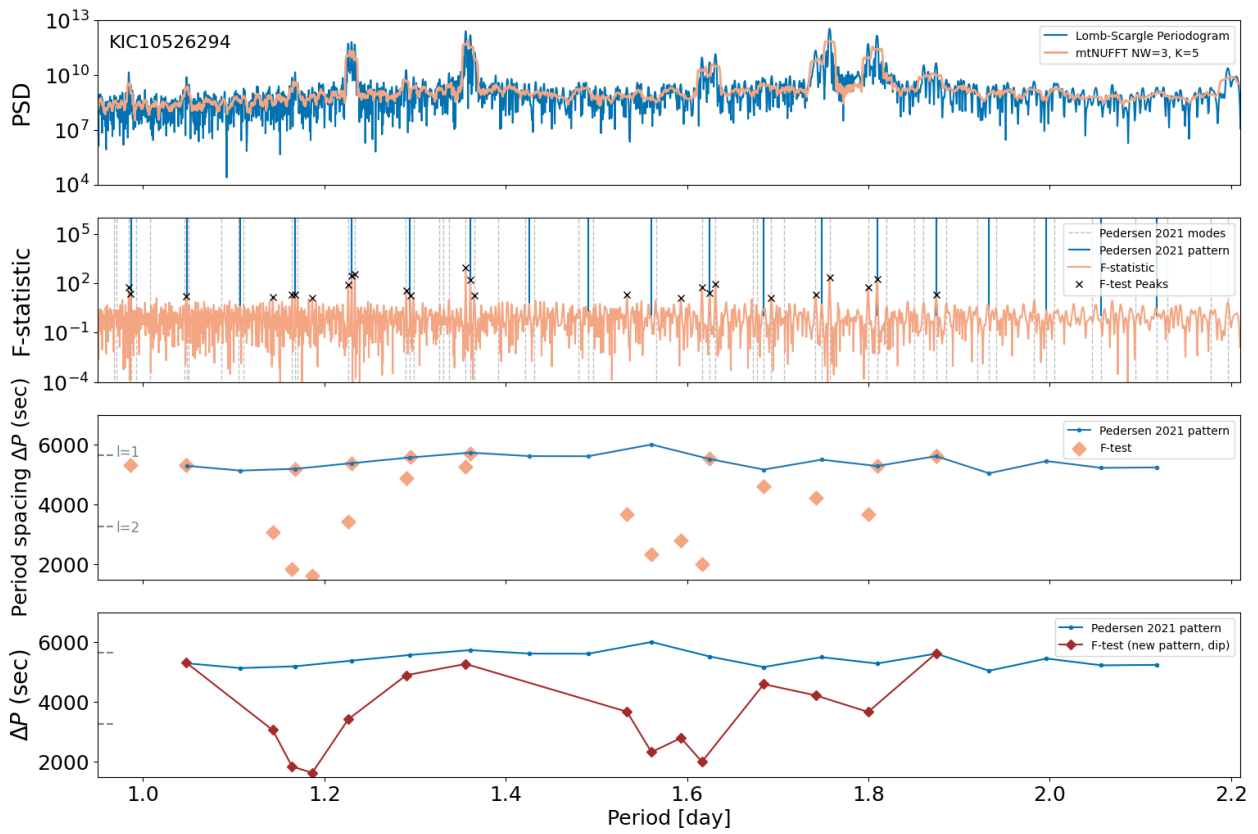


Fig. A.19. Comparison of our F-test detections with the period spacing patterns in PD21 for KIC10526294.

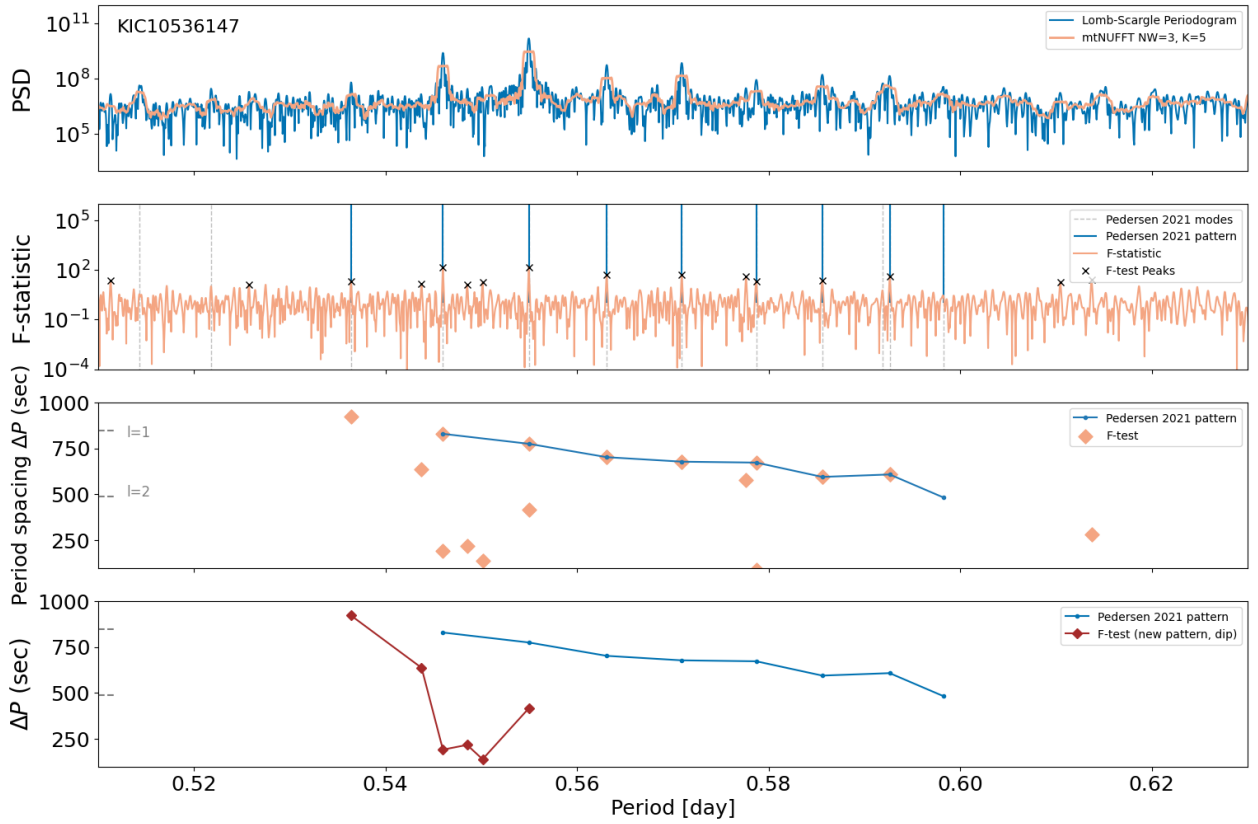


Fig. A.20. Comparison of our F-test detections with the period spacing patterns in PD21 for KIC10536147.

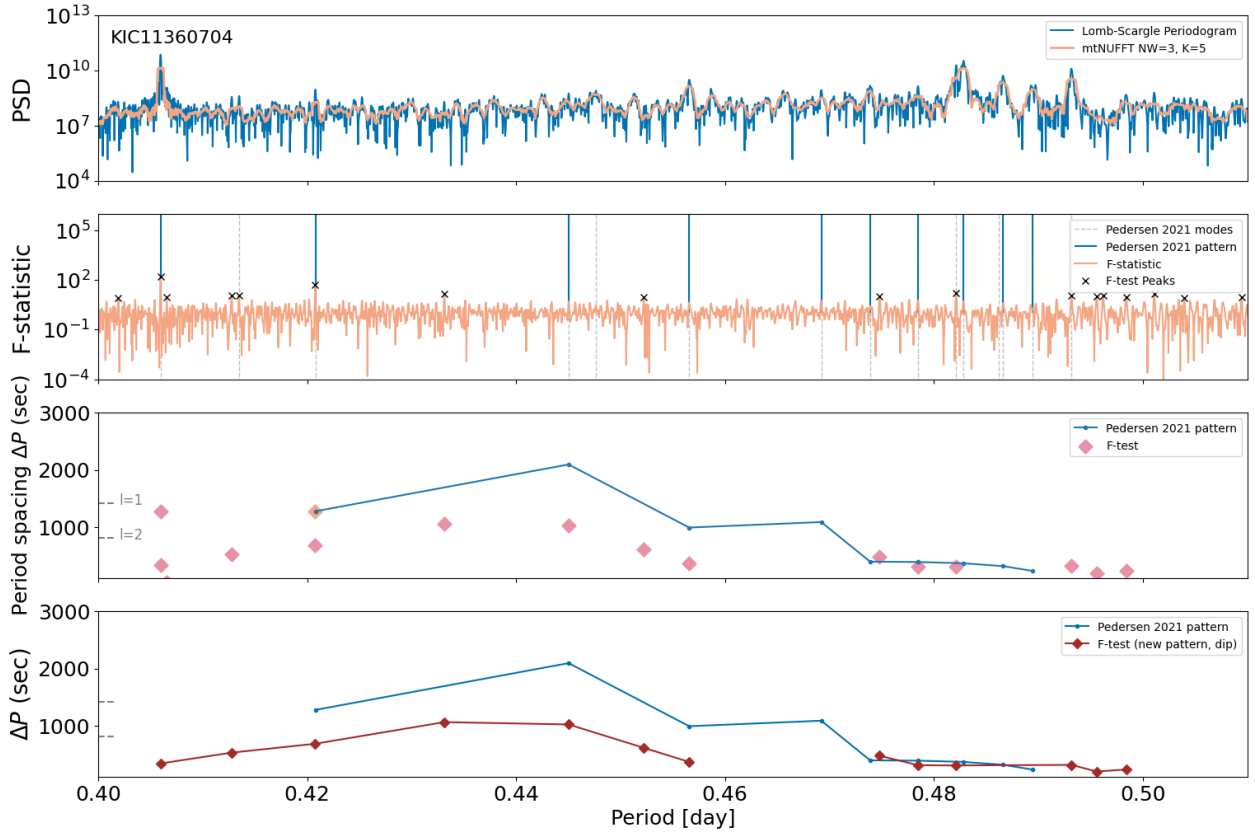


Fig. A.21. Comparison of our F-test detections with the period spacing patterns in PD21 for KIC11360704.

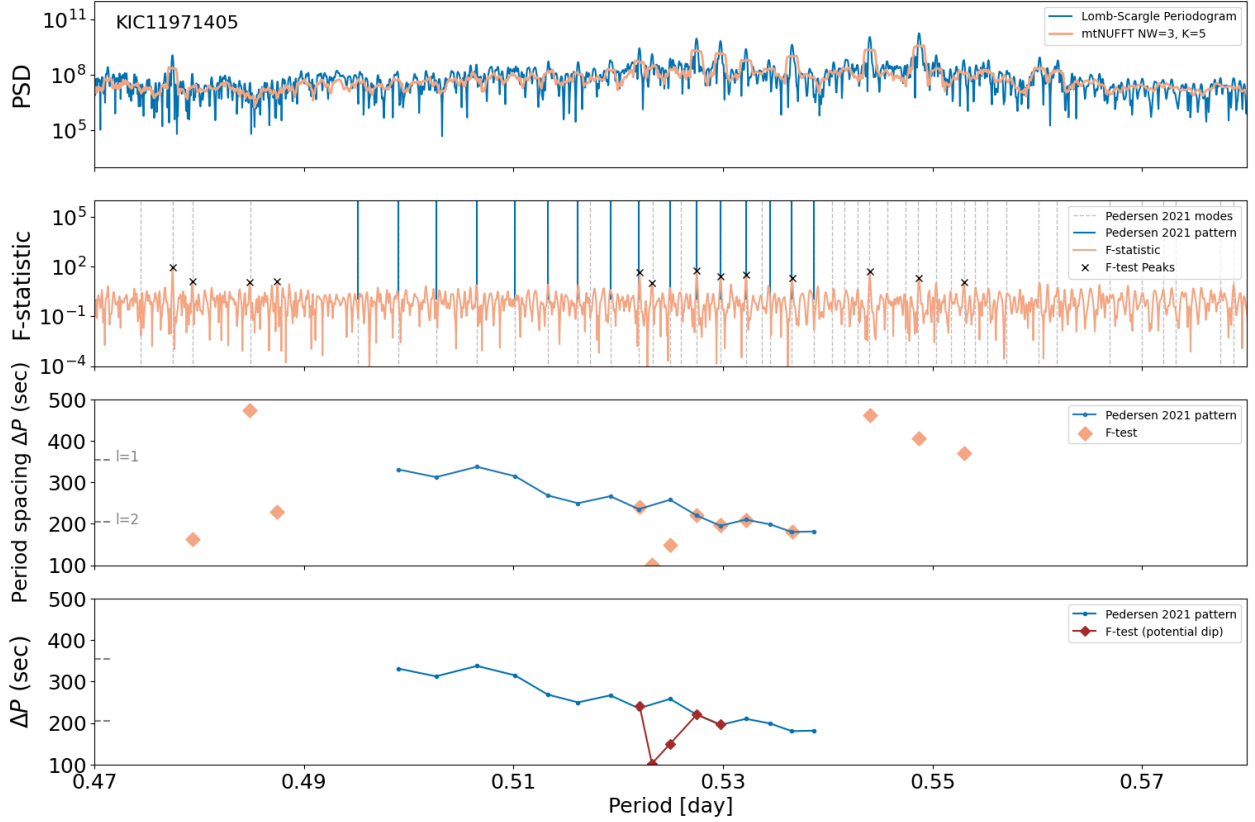


Fig. A.22. Comparison of our F-test detections with the period spacing patterns in PD21 for KIC11971405.